

Puneet Jain

puneetjain2606 (at) gmail.com

s1620011 (at) jaist.ac.jp

Skype: puneet.jain451

Japan Advanced Institute of Science and Technology (JAIST)
8-316, JAIST Student Housing, 1-8 Asahadai,
Nomi-city, Ishikawa
923-1211, Japan
+81-761-51-1517

EDUCATION

Japan Advanced Institute of Science and Technology (JAIST) Ph.D. Thesis: “Investigation of In ₂ O ₃ -based Oxide Films by Direct Imprinting for TFT Applications” <u>Supervisor:</u> Prof. Eisuke Tokumitsu (<i>Final defense passed and waiting for degree ceremony</i>)	Nomi, Japan 2016 – 09/2019 (expected)
Amity University , Amity Institute of Nanotechnology M. Tech. (Nanotechnology) [<u>CGPA</u> : 9.02/10] Thesis: “Silica Nanoparticle Synthesis and Patterning by Soft Lithography”	Noida, India 2012 - 2014
Jamia Millia Islamia University , Department of Applied Sciences & Humanities M.Sc. (Electronics) [<u>%</u> : 81.88]	Delhi, India 2008 - 2010
Delhi University , Department of Electronics B.Sc. (Electronics) [<u>%</u> : 72.66]	Delhi, India 2005 - 2008
Gita Bal Niketan Sr. Sec. School Class XII, C.B.S.E Board [<u>%</u> : 78.60]	Faridabad, India 2004-2005
Gita Bal Niketan Sr. Sec. School Class X, C.B.S.E Board [<u>%</u> : 75.40]	Faridabad, India 2002-2003

WORK EXPERIENCE

Indian Institute of Information Technology Research Fellow	Allahabad, India December 2014 – March 2016
Tata Motors Ltd. Process Executive (services)	Gurgaon, India October 2010 – April 2012

PUBLICATION(s)

◇ **Published Papers**

- “Electrical Properties of In₂O₃ and ITO Thin Films Formed by Solution Process using In(acac)₃ Precursors”, **Puneet Jain**, Yuji Nakabayashi, Ken-ichi Haga, and Eisuke Tokumitsu (submitted in Japanese Journal of Applied Physics).
- “Electrical and Patterning Properties of Indium Oxide (In₂O₃) and Indium Tin Oxide (ITO) by Direct Nanoimprinting Technique”, **Puneet Jain**, Chang Su, Ken-ichi Haga and Eisuke Tokumitsu, *Jpn. J. Appl. Phys.*, **58** SDDJ05 (2019).

- “Dependences of Deposition Rate and OH Content on Concentration of Added Trichloroethylene in Low-Temperature Silicon Oxide Films Deposited Using Silicone Oil and Ozone Gas”, Susumu Horita and **Puneet Jain**, *Jpn. J. Appl. Phys.*, **57** 03DA02 (2018).
- “Effect of Trichloroethylene Enhancement on Deposition Rate of Low-Temperature Silicon Oxide Films by Silicone Oil and Ozone”, Susumu Horita and **Puneet Jain**, *Jpn. J. Appl. Phys.*, **56** 088003 (2017).
- “Comparative Study of Co₂MnSi Structural and Surface Morphological Thin Films on Si/SiO₂”, Rashmi Singh, **Puneet Jain**, Naresh Kumar, Rachana Kumar, Pramod Kumar, *Adv. Mat. Proce.*, **2(2)** 76 (2017).
- “Radius Ratio Rule for Surface Hydrophilization of Polydimethylsiloxane and Silica Nanoparticle Composite”, Vijaykumar Toutam, **Puneet Jain**, Rina Sharma, Sivaiah Bathula, and Ajay Dhar, *Appl. Surf. Sci.*, **349** 196 (2015).

◇ Presentations

International conferences

- “Hall Mobility and Carrier Concentration of In(acac)₃ Precursor Derived Solution Processed In₂O₃ and ITO Thin Films”, **Puneet Jain**, Ken-ichi Haga, and Eisuke Tokumitsu, The 7th International Symposium on Organic and Inorganic Electronic Materials and Related Nanotechnologies (EM-Nano’ 19), June 19-22, 2019, Shinshu University, Nagano, Japan (poster).
- “Electrical Properties of In₂O₃ and In-Sn-O Films Prepared by Direct Nanoimprinting”, **Puneet Jain**, Ken-ichi Haga, and Eisuke Tokumitsu, The 31st International Microprocessor and Nanotechnology Conference (MNC’ 18), November 13-16, 2018, Sapporo Park Hotel, Sapporo, Japan (poster).
- “Effect of Trichloroethene (TCE) on Deposition Rate and Film Quality of Low-Temperature SiO₂ Films Grown Using Silicone Oil and Ozone Gas”, **Puneet Jain** and Susumu Horita, The 24th International Workshop on Active-Matrix Flat Panel Displays and Devices (AM-FPD’ 17), July 4-7, 2017, Ryukoku University, Avanti Kyoto Hall, Kyoto, Japan (oral).
- “Catalytic Effect of Trichloroethene on Deposition Rate of Silicon Oxides Films Deposited by APCVD Using Silicone Oil and Ozone Gas”, **Puneet Jain** and Susumu Horita, The 23rd International Display Workshop (IDW’ 16), December 7-9, 2016, Fukuoka International Congress Center, Fukuoka, Japan (oral).

Domestic conferences

- “Electrical Properties of In₂O₃ and ITO Thin Films Prepared by Solution Process using In(acac)₃ Precursor”, **Puneet Jain**, Ken-ichi Haga, and Eisuke Tokumitsu, Japan Society of Applied Physics (JSAP 66th Spring Meeting’ 19), March 9-12, 2019, Tokyo, Japan (poster).
- “Direct Imprinting and Electrical Properties of ITO Precursor gel”, **Puneet Jain**, Ken-ichi Haga, and Eisuke Tokumitsu, Japan Society of Applied Physics (JSAP 65th Spring Meeting’ 18), March 17-20, 2018, Tokyo, Japan (oral).
- “Study of Electrical and Imprinting Properties of ITO Precursor Gel using Direct Imprinting”, **Puneet Jain**, Chang Su, Ken-ichi Haga, and Eisuke Tokumitsu, Japan Advanced Institute of Science and Technology (JAIST) Japan-India Symposium, March 5-6, 2018, JAIST, Japan (poster).
- “Trichloroethene Concentration Effect on Deposition Rate and Properties of Low-Temperature Grown SiO₂ Films by using Silicone Oil and Ozone Gas”, **Puneet Jain** and Susumu Horita, Japan Society of Applied Physics (JSAP 64th Spring Meeting’ 17), March 14-17, 2017, Yokohama, Japan (poster).
- “Effect of Adding Organic Solution on the Deposition Rate and Quality of Silicon Oxide Films using Silicone Oil and Ozone Gas”, **Puneet Jain** and Susumu Horita, Thin-Film Materials and Devices (TFMD’ 16), October 21-22, 2016, Kyoto, Japan (poster).

- “Effect of Added Organic Solution on Low-Temperature Deposition of SiO_x Films by APCVD using Silicone Oil and Ozone Gas”, **Puneet Jain** and Susumu Horita, Japan Society of Applied Physics (JSAP, 77th Autumn Meeting’ 16), September 13-16, 2016, Niigata, Japan (poster).

SCIENTIFIC EQUIPMENTS KNOWN

- Experience on use of clean room [*class-10 and 100*]
- Atmospheric pressure chemical vapor deposition (APCVD) [detailed experience]
- Alpha-step thickness measurement profilometer [*KLA Tencor; Alphastep D-500*]
- Atomic force microscopy [*SII SPI3800, SPA-400; SII-Hitachi*]
- Desktop SEM [*TM3030 Plus; Hitachi*]
- Fourier transform infrared spectrometer (FTIR) [*Spectrum 100 FT-IR Spectrometer; Perkin Elmer*]
- Hall measurement set-up [*Resitest 8400; TOYO Corporation*]
- Monochromatic ellipsometry
- Photolithography set-up
- Rapid thermal annealing (RTA)
- Scanning electron microscope (SEM) [*S-4100, S-4500; Hitachi*]
- Spin-coater
- X-ray diffraction [*X’Pert PRO MRD Epi; PANalytical*]
- X-ray photoelectron spectroscopy (XPS) [*S-probe*]

ACHIEVEMENT(s)

1. Got a score of 880/990 in TOEIC (Test of English for International Communication).
2. Got a band of 6 in IELTS (International English Language Testing Scheme).

REFERENCES

1. **Prof. Eisuke Tokumitsu (Professor; JAIST, Japan)**
Email: e-toku (at) jaist.ac.jp
2. **Dr. Rina Sharma (Sr. Principal Scientist; National Physical Laboratory, Delhi, India)**
Email: rina (at) nplindia.org

I hereby declare that the above information is true and correct to the best of my knowledge and belief.

Puneet Jain

REGULAR PAPER

Electrical and patterning properties of direct nanoimprinted indium oxide (In_2O_3) and indium tin oxide (ITO)

To cite this article: Puneet Jain *et al* 2019 *Jpn. J. Appl. Phys.* **58** SDDJ05

View the [article online](#) for updates and enhancements.



Electrical and patterning properties of direct nanoimprinted indium oxide (In_2O_3) and indium tin oxide (ITO)

Puneet Jain*, Chang Su, Ken-ichi Haga, and Eisuke Tokumitsu

School of Materials Science, Japan Advanced Institute of Science and Technology (JAIST), Nomi-shi, Ishikawa 923-1292, Japan

*E-mail: s1620011@jaist.ac.jp

Received November 27, 2018; accepted February 7, 2019; published online May 9, 2019

The electrical and patterning properties of direct imprinted indium oxide (In_2O_3) and indium tin oxide (ITO) precursor gel films have been studied. The electrical properties of the imprinted films have also been compared with the electrical properties of non-imprinted films. In_2O_3 and ITO have almost the same type of solutes in solution but In_2O_3 shows better patterns than ITO, that is, the addition of tin to In_2O_3 causes the patterns to degrade because ITO has a lower $\tan \delta$ during viscoelastic measurements than In_2O_3 . In addition, the electrical properties (i.e. Hall mobility and carrier concentration) of In_2O_3 were affected by the direct imprinting process while the effects were not pronounced for ITO films.

© 2019 The Japan Society of Applied Physics

1. Introduction

Printed electronics have recently gained attention due to their low environmental impact, fewer fabrication steps, large area fabrication, ease of patterning on organic and inorganic substrates and low cost.^{1–4} Some of the current printing techniques include inkjet printing, offset printing, microcontact printing and gravure printing; these techniques are used to fabricate printed electronics, organic thin film transistors (TFTs),^{5,6} printed circuits,⁷ sensors^{6–8} and displays.⁹ Inkjet printing is a popular method, but is not appropriate for the miniaturization of advanced electronic devices as the required resolution is sub-micrometers or less¹⁰ which cannot be realized by inkjet printing. Furthermore, it is hard to achieve precise shape control of the film via inkjet printing.¹¹

A novel printing technique known as nano-rheology printing (n-RP),^{4,12–15} based on direct imprinting of precursor gel films, can fabricate patterns as small as 100 nm with good shape control. The study of the rheological properties of a material in a confined geometry is known as nano-rheology, while rheology itself is concerned with the deformation and flow of matter.¹³ n-RP is a resist-free, direct printing method which utilizes the rheological properties of a metal-oxide precursor gel to form patterns in the precursor gel. Other advantages of n-RP are the simple equipment with less complex production steps and less wastage of materials. Although the complete process is described elsewhere,^{4,12} a brief summary of the n-RP process is illustrated in Fig. 1. First, the source solution (i.e. the source solution of the metal-oxide material in which the patterns are to be created) is spin-coated on the substrate and then dried, so that the source solution on the substrate can be changed from a liquid film into an oxide precursor gel film as shown in Fig. 1(a). The sample (i.e. the substrate with precursor gel) is then inserted into the n-RP machine and aligned properly with respect to the mold [Fig. 1(b)]. The mold is then applied directly (without any resist) on the precursor gel, after which appropriate imprinting temperature and pressure are applied [Fig. 1(c)]. The oxide precursor gel softens at the imprinting temperature, thereby allowing the transfer of patterns from the mold to the gel film. The mold and gel are allowed to be in contact with each other for some time, after which the sample is cooled gradually. The mold is then detached from the patterned gel film [Fig. 1(d)], with some residual film

remaining on the gel film, corresponding to the convex regions of the mold. The residual film is removed by dry etching. During this dry etching, there is also slight etching of the thick patterned regions that correspond to the concave patterns of the mold [Fig. 1(e)]. Finally, after annealing, the etched patterned gel film oxidizes into the required oxide material [Fig. 1(f)].

To date, fine pattern formation by n-RP has been reported for In_2O_3 ,⁴ ITO,⁴ ruthenium lanthanum oxide (RuLaO)¹⁶ and ruthenium oxide (RuO).¹⁷ However, there have been few studies of the electrical properties of In_2O_3 and ITO films prepared by n-RP (sometimes also referred to as direct imprinting in this work). In the present work, we report the electrical properties of In_2O_3 and ITO films imprinted by the n-RP process along with the patterning properties. In_2O_3 and ITO were selected because they are very mature materials used as a channel in TFTs and transparent conducting electrodes for solar cells, flat panel displays, etc.^{18–20} The electrical properties of imprinted In_2O_3 and ITO films were also compared with those of non-imprinted films. In addition, in the previous work on the patterning properties of ITO, the ITO film was prepared using indium acetylacetonate and tin acetylacetonate in propionic acid. In the present work, tin chloride (SnCl_2) was also used to prepare ITO along with tin acetylacetonate.

2. Experimental methods

First, the patterning and electrical properties of In_2O_3 by n-RP were investigated to determine appropriate patterns; these conditions were then used as reference conditions to investigate the n-RP properties in ITO films, i.e. to study the effect of the addition of tin (Sn) on In_2O_3 patterning and electrical properties. The In_2O_3 source solution was prepared by dissolving indium(III) acetylacetonate [$\text{In}(\text{acac})_3$, Wako Pure Chemicals] in propionic acid ($\text{C}_2\text{H}_5\text{COOH}$, hereinafter called PrA; Kanto Chemicals), while source solutions of ITO were prepared using two different precursors of Sn, keeping $\text{In}(\text{acac})_3$ and PrA the same, that is, two precursor materials were used to make the source solution of ITO, one was tin(II) acetylacetonate [$\text{Sn}(\text{acac})_2$, Sigma-Aldrich] and the other was SnCl_2 (Wako Pure Chemicals). So, one source solution of ITO was prepared using $\text{Sn}(\text{acac})_2$ and $\text{In}(\text{acac})_3$ in PrA [hereinafter called ITO via $\text{Sn}(\text{acac})_2$] and the other source solution was prepared using SnCl_2 and $\text{In}(\text{acac})_3$ in PrA

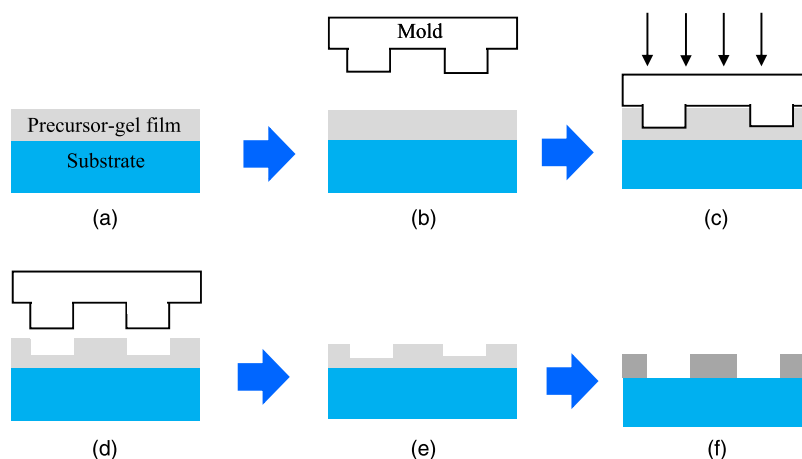


Fig. 1. (Color online) Schematic of the n-RP process.

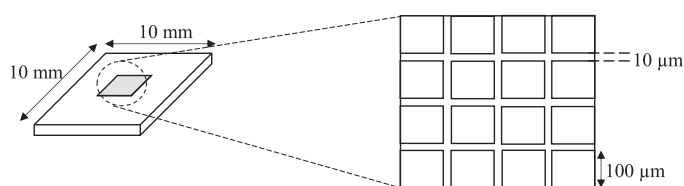


Fig. 2. Schematic of the SNP-O2 quartz mold.

[hereinafter called ITO via SnCl_2]. The Sn content of both prepared ITO source solutions was 10 wt%.

To study the n-RP properties of In_2O_3 , the In_2O_3 source solution was first spin-coated on a $\text{SiO}_2(200\text{ nm})/\text{Si}$ substrate (hereinafter called SiO_2/Si), then it was dried in air at 100°C for 3 min to evaporate the solvent to form an In_2O_3 precursor gel (hereinafter called In_2O_3 gel film). Next, the gel film was inserted into an n-RP machine and imprinting was performed as shown in Fig. 1. The imprinting temperature was maintained for 5 min, keeping the mold and gel film intact. The applied pressure was 15 MPa (for a $10\text{ mm} \times 10\text{ mm}$ mold and 1500 N force) and the imprinting temperature was around 175°C . After 5 min, the sample was cooled gradually and when the temperature reached 90°C the mold was detached and the sample was removed from the n-RP machine. Two different types of molds were used in this work, and are discussed later in this section. The above-mentioned conditions were used as reference conditions to study the patterning and electrical properties of ITO [hereinafter ITO means ITO via SnCl_2 and ITO via $\text{Sn}(\text{acac})_2$, unless otherwise stated].

The patterns were checked using an optical microscope and further characterization was performed by secondary ion mass spectroscopy (SIMS; Material Science and Technology, Promotion Foundation Analysis, Japan), Fourier transform infrared spectroscopy (FT-IR; Perkin Elmer Spectrum 100 FT-IR Spectrometer) in transmittance mode and X-ray photoelectron spectroscopy (XPS; S-Probe Surface Spectrometer). The crystallinity of the films was measured by an X-ray diffractometer (XRD; X'Pert PRO MRD, PANalytical) using $\text{Cu K}\alpha$ radiation ($\lambda = 1.5405\text{ \AA}$) with an acceleration voltage of 40 kV and a current of 40 mA. The thermal behavior (i.e. evaporation of the solvent, decomposition of organic species and oxidation of the precursor gel) of the samples was studied via

thermogravimetry–differential thermal analysis (TG-DTA; Toshiba Nanoanalysis Corporation). For mass spectroscopy and study of the viscoelastic properties, a Fourier transform ion cyclotron resonance mass spectrometer (FT-ICR-MS; Solarix-JA, Bruker Daltonics) and Rheogel E-4000 (UBM Corporation) were used, respectively. For the measurement of electrical properties, a Hall effect measurement system (TOYO Corporation, Resitest 8400) was utilized at room temperature with the van der Pauw method. The annealing was done using rapid thermal annealing (RTA; Ulvac Sinku-Riko Infrared Furnace).

A “quartz SNP-O2” mold ($10\text{ mm} \times 10\text{ mm} \times 0.625\text{ mm}$) purchased from NTT-Advanced Technology was used to study the patterning properties. SNP-O2 is a checker mold with square concave patterns with an area of $100\text{ }\mu\text{m}^2$ and a depth of 500 nm. Furthermore, each square is separated from every other square by a $10\text{-}\mu\text{m}$ -wide convex line. A schematic of the SNP-O2 quartz mold is shown in Fig. 2.

A “flat” mold, made of Eagle XG glass purchased from Corning, with an area of $10\text{ mm} \times 10\text{ mm}$ and thickness of 1.1 mm was used to study the electrical properties because a large imprinted area is necessary for Hall measurements.

3. Results and discussion

3.1. Results

3.1.1. Patterning properties. The patterns of In_2O_3 , ITO via $\text{Sn}(\text{acac})_2$ and ITO via SnCl_2 using the SNP-O2 mold (as described in Sect. 2) are shown in Fig. 3. It was evident that the patterns of In_2O_3 were better than those of ITO and that they degraded with the addition of Sn.

Figures 4 and 5 show the TG and DTA of the source solutions, respectively. TG-DTA measurements were performed in air at a constant heating rate of $10^\circ\text{C min}^{-1}$. It can be seen from the TG-DTA curves that the evaporation of the

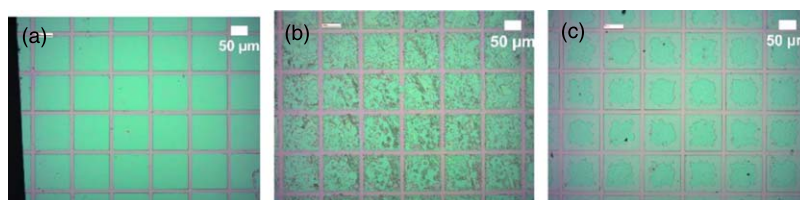


Fig. 3. (Color online) Optical microscope images of nano-rheology printed (a) In_2O_3 , (b) ITO via $\text{Sn}(\text{acac})_2$ and (c) ITO via SnCl_2 .

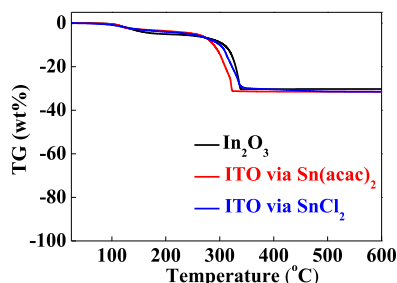


Fig. 4 (Color online) Thermogravimetric (TG) analysis of In_2O_3 and ITO solutions.

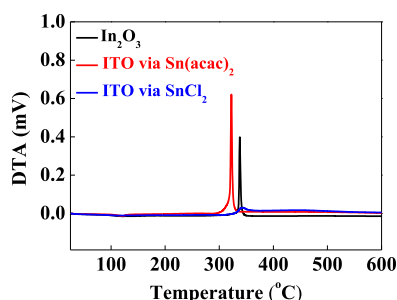


Fig. 5. (Color online) Differential thermal analysis (DTA) of In_2O_3 and ITO solutions.

solvent in In_2O_3 and ITO is complete at around 100 °C. Around this temperature, semi-solid substances (i.e. oxide precursor gels) are generated; an exothermic reaction starts at 290 °C, ending at around 350 °C. The exothermic peak indicates the solidification of each oxide precursor gel due to oxidation. From TG-DTA analysis, it was evident that the gel state of In_2O_3 and ITO is in the temperature range between 100 °C to 290 °C, so imprinting was performed in this temperature range as the specimen will be in a semi-solid state.

3.1.2. Electrical properties. Before going further, it is necessary to explain two terms—imprinted and non-imprinted film. After the gel film was prepared on the SiO_2/Si wafer, the sample (i.e. a substrate having a precursor gel film) was inserted into the imprinting machine and imprinting was performed on a small region of the sample (i.e. pressure was applied on a small region of the gel, while the complete sample experienced the same imprinting temperature). After imprinting, the sample was taken out of the machine and cut into two parts. The part with pressure applied is called the “imprinted film” while the part without applied pressure is the “non-imprinted film”. For the electrical properties, the Hall mobility and carrier concentration of “imprinted In_2O_3 and ITO films” were compared with “non-imprinted In_2O_3 and ITO films”. Figure 6 shows the Hall mobility and carrier concentration of imprinted and non-imprinted In_2O_3 and ITO annealed at 600 °C in an O_2 environment for 1 h. The

Hall mobilities of the 600 °C annealed films were reduced by the direct imprinting process which was performed at 175 °C. For In_2O_3 , the reduction of mobility caused by the imprinting process is more serious than in ITO. The carrier concentrations of non-imprinted and imprinted In_2O_3 films were $4.2 \times 10^{18} \text{ cm}^{-3}$ and $2.8 \times 10^{19} \text{ cm}^{-3}$, respectively, suggesting that the imprinted In_2O_3 film contains more oxygen vacancies, whereas the carrier concentration of the ITO films were almost the same, regardless of the Sn precursor.

3.2. Discussion

The organic species in the gel films were analyzed by FT-IR, as shown in Fig. 7, where most peaks were due to carbon-related compounds. In the FT-IR spectra the broad band at around 3440 cm^{-1} and the peak at around 2970 cm^{-1} are due to the stretching vibration of O–H and C–H bonds, respectively.²¹⁾ Around 1560 cm^{-1} , the peak, labeled by (a) in Fig. 7, is due to the acetylacetonato band in the In complex²¹⁾ (which some authors refer to as COO^- asymmetric stretching).²²⁾ The peaks at around 1470, 1430 and 1380 cm^{-1} are due to C–H bending, those at around 1250, 1140 and 1080 cm^{-1} are due to C–H stretching,²³⁾ those at around 1015 cm^{-1} (labeled as (b) in the figure) are due to the acetylacetonato band in the In complex²²⁾ (which some authors report as a C=O bond)²³⁾ and the peaks at 888 and 814 cm^{-1} are due to C–H bending.^{21,24)} The peaks at around 670 cm^{-1} are due to the In–O bond²²⁾ and those around 600 cm^{-1} are due to Sn–O,^{24–26)} (also shown in Fig. 7 labeled by (c) and (d), respectively). The FT-IR measurement in Fig. 7 shows that In_2O_3 has a relatively larger number of organic species than ITO. A relatively smaller number of organic species in ITO compared to In_2O_3 may be one of the reasons for the degradation of patterning properties in ITO; as stated in Ref. 16, the gel should have a high content of organic species to soften easily for good patterning properties. The film thickness of the gel films measured by an alpha-step profilometer are similar: In_2O_3 , 273 nm; ITO via SnCl_2 , 280 nm; ITO via $\text{Sn}(\text{acac})_2$, 243 nm. Since the film thicknesses are approximately same, this means that from the very beginning there are more organic species in In_2O_3 than in ITO.

The composition of the source solutions was further studied using cryospray ionization Fourier transform ion cyclotron resonance mass spectroscopy (CSI-FT-ICR-MS). The mass spectra resulting from the positive mode measurements are shown in Fig. 8 and the inset shows the mass spectra for m/z values from 0 to 500 on a semi-log scale because these peaks are hardly visible on the linear scale. Figure 8 shows that most solutes have the general formula $\text{In}_n(\text{acac})_2(\text{PrA})_x(\text{CH}_3\text{O})_y$, where $n = 1-7$, x and y are positive integers, “PrA” is the propionate ligand ($\text{CH}_3\text{CH}_2\text{COO}^-$) and “acac” is the acetylacetonate ligand ($\text{OCCH}_3\text{CHOCCH}_3^-$). CH_3O (or $-\text{CH}_2\text{OH}$) is the attachment of methanol to the

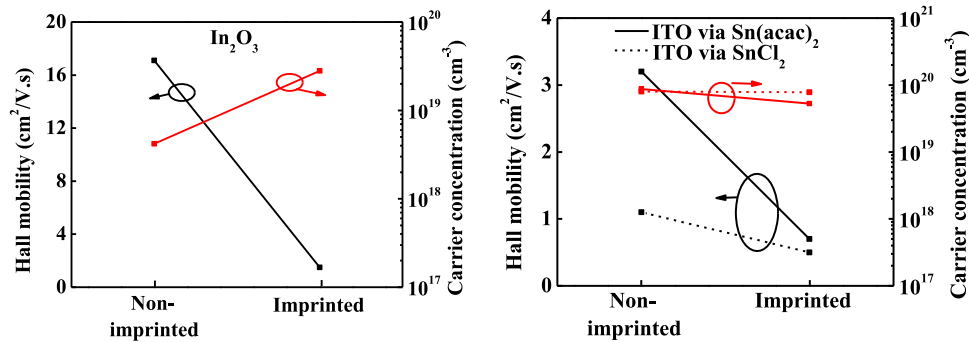


Fig. 6. (Color online) Hall mobility of imprinted and non-imprinted films after annealing at 600 °C.

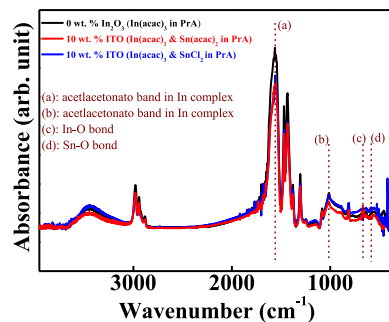


Fig. 7. (Color online) FT-IR spectra of In₂O₃ and ITO.

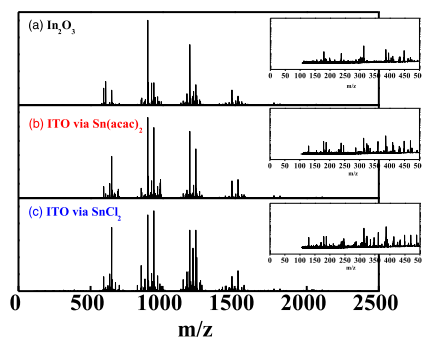


Fig. 8. (Color online) CSI-FT-ICR-MS analysis of (a) In₂O₃, (b) ITO via Sn(acac)₂ and (c) ITO via SnCl₂.

solution because the source solutions were diluted with methanol for mass spectral analysis. The general formula suggests that the solute is mostly made up of a combination of In(acac)₃ molecules and propionic acid molecules through van der Waals forces, which can also be stated as: In (indium) forms a basic structure with one In atom coordinated by two acac. The mass spectra show that In₂O₃ and ITO possess peaks at the same m/z value, but the intensities are different, with a common pattern, as shown in Table I.

From the mass spectra, it is evident that In₂O₃, ITO via Sn(acac)₂ and ITO via SnCl₂ have almost the same solute structures, except for SnCl₂ where there was a peak containing Cl at the higher m/z value. Similarly, more peaks containing In and organics along with Cl, Cl and Sn, or Sn are expected at higher m/z values. Although they have similar solute structures, the patterns degraded (as shown in Fig. 3) with the addition of Sn, because In₂O₃ shows viscoelastic changes similar to glass transition (as in the case of polymers) while the viscoelastic properties are modified with the addition of Sn, as shown in Fig. 9, which shows the viscoelastic properties of the semi-solid pellet of In₂O₃ and

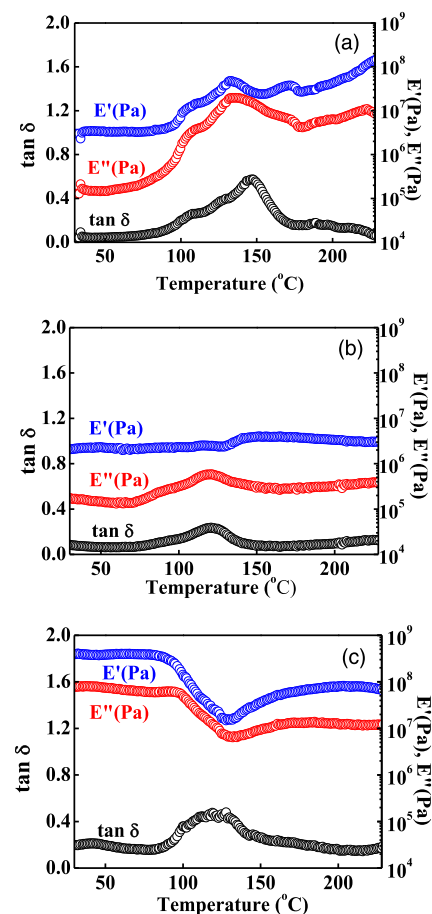


Fig. 9. (Color online) Viscoelastic properties of (a) In₂O₃, (b) ITO via Sn(acac)₂ and (c) ITO via SnCl₂.

ITO. The viscoelastic properties were measured using a rheometer, in which the sample was sandwiched between two clips. The measurements were performed using dynamic viscoelastic measurement with sine waves in the temperature dependence mode (i.e. the oscillatory mode). The sample was fabricated by drop-casting the In₂O₃/ITO solution onto a glass Petri dish, then heating it at 100 °C in air and finally pulverizing it from the Petri dish. The obtained semi-solid powder was formed in a shape of a pellet (1 mm thick) at room temperature using a compression-molding machine.

From Fig. 9 it can be seen that tan δ for In₂O₃ is higher than for ITO, which means that the In₂O₃ gel becomes softer at a certain temperature than ITO. Hence, it can be concluded that In₂O₃ shows better viscoelastic transformation under pressure and temperature than ITO, which may explain the

Table I. Structures corresponding to m/z values for In_2O_3 and ITO.

In_2O_3 (A)		ITO via $\text{Sn}(\text{acac})_2$ (B)		ITO via SnCl_2 (C)		Structure
Experimental mass	Theoretical mass	Experimental mass	Theoretical mass	Experimental mass	Theoretical mass	
312.99	312.99	312.99	312.99	312.99	312.99	$\text{In}(\text{acac})_2$
646.98	646.98	646.98	646.98	646.98	646.98	$\text{In}_2(\text{acac})_2(\text{PrA})_3$
980.98	980.97	980.98	980.97	980.98	980.97	$\text{In}_3(\text{acac})_2(\text{PrA})_6$
1230.94	1230.94	1230.95	1230.94	1230.95	1230.94	$\text{In}_4(\text{acac})_2(\text{PrA})_7(\text{CH}_3\text{O})_2$
1480.91	1480.91	1480.92	1480.91	1480.92	1480.91	$\text{In}_5(\text{acac})_2(\text{PrA})_8(\text{CH}_3\text{O})_4$
1730.89	1730.88	1730.89	1730.88	1730.85	1730.8537	$\text{In}_6(\text{acac})_2(\text{PrA})_9(\text{CH}_3\text{O})_6$, for A and B; $\text{In}_6(\text{acac})_6(\text{PrA})_5(\text{CH}_3\text{O})(\text{CH}_3)\text{HCl}$, for C
604.97	604.97	604.97	604.97	604.97	604.97	$\text{In}_2(\text{acac})_2(\text{PrA})_2(\text{CH}_3\text{O})$
938.96	938.96	938.96	938.96	938.96	938.96	$\text{In}_3(\text{acac})_2(\text{PrA})_5(\text{CH}_3\text{O})$
1272.96	1272.95	1272.96	1272.95	1272.96	1272.95	$\text{In}_4(\text{acac})_2(\text{PrA})_8(\text{CH}_3\text{O})$
1522.93	1522.92	1522.93	1522.92	1522.93	1522.92	$\text{In}_5(\text{acac})_2(\text{PrA})_8(\text{CH}_3\text{O})$
1772.90	1772.89	1772.90	1772.89	1772.90	1772.90	$\text{In}_6(\text{acac})_2(\text{PrA})_{10}(\text{CH}_3\text{O})_5$, for A and B; $\text{In}_6(\text{acac})_6(\text{PrA})_5(\text{CH}_3\text{O})(\text{C}_4\text{H}_9)\text{HCl}$, for C
2022.87	2022.86	—	—	—	—	$\text{In}_7(\text{acac})_2(\text{PrA})_{11}(\text{CH}_3\text{O})_7$

$\text{PrA} = \text{C}_2\text{H}_5\text{COO}^-$; $\text{acac} = \text{C}_5\text{H}_7\text{COO}^-$.

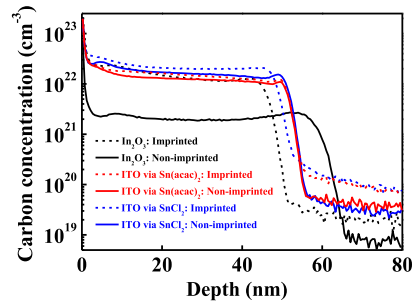


Fig. 10. (Color online) SIMS profile of imprinted and non-imprinted In_2O_3 and ITO after annealing.

degradation of patterns with the addition of Sn in n-RP experiments.

To study the effect of direct imprinting on the electrical properties of films annealed at 600 °C, SIMS measurement was performed and the results are shown in Fig. 10. The carbon concentration in the imprinted In_2O_3 was more than that in non-imprinted In_2O_3 films, but in ITO the carbon concentration was almost the same for imprinted and non-imprinted films. Indium precursor [i.e. $\text{In}(\text{acac})_3$] and the solvent (i.e. PrA) are themselves the sources of carbon in the films.

The imprinting temperature in this experiment was 175 °C, and at this temperature the organic species in the precursor gel film (such as PrA, acac) try to evaporate from the film. However, at the same time, the films were under pressure (i.e. imprinting pressure), thereby preventing evaporation of the

organic species to some extent. It is interesting to note that the carbon concentration is higher for the imprinted film than the non-imprinted film, even though the films were annealed at 600 °C in oxygen ambient after the imprinting process. These trapped carbons act as scattering centers that lead to a reduction in the mobility of the films in the case for In_2O_3 , whereas the ITO gel shows less effect of imprinting pressure on the residual carbon concentration due to its lower $\tan \delta$ value, which corresponds to the experimental result that reduction of Hall mobility is not so pronounced for ITO.

As shown in Fig. 6, the carrier concentration in In_2O_3 is increased by the imprinting process but does not change much in ITO, which corresponds to the fact that the precursor gel does not deform as much in ITO as in In_2O_3 . This deformation may create oxygen vacancies, which are a source of carrier concentration in In_2O_3 and ITO.^{27–29)} To confirm this, the chemical bonding was studied using XPS, as shown in Fig. 11, where the x-axis represents the intensity (arbitrary units) and the y-axis represents binding energy (eV). The XPS peaks were calibrated using a binding energy of 284.6 eV for carbon. The oxygen 1s peak has been deconvoluted into three positions: a lower binding energy due to metal-oxide bonds (M-O bond), a medium binding energy due to oxygen vacancies (O vacancy) and a higher binding energy due to oxygen of the free hydroxyl group (OH bonds), which is caused by the water molecules absorbed on the surface.³⁰⁾ To understand the difference between samples, the peak area ratio (O vacancy/M-O bond) was calculated as a measure of the formation of oxygen

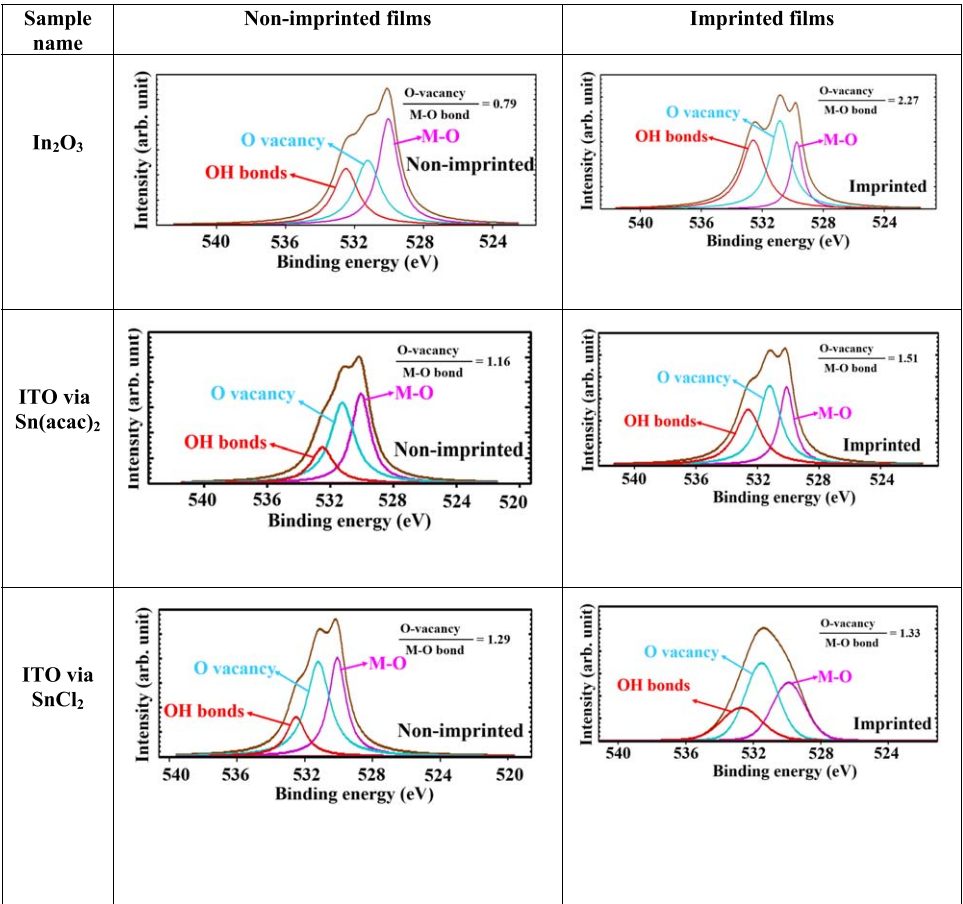


Fig. 11. (Color online) XPS spectra of indium oxide and ITO for the oxygen 1s peak.

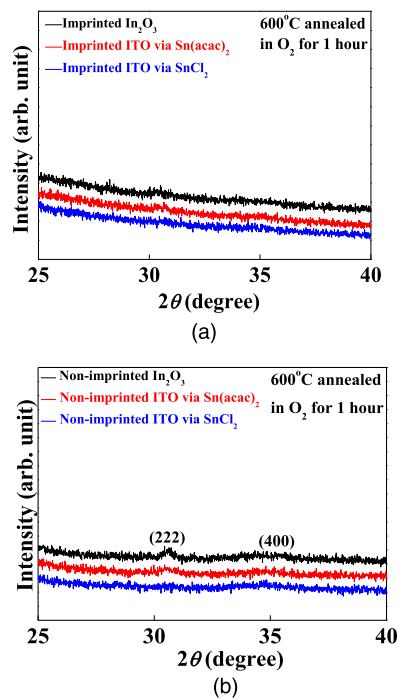


Fig. 12 (Color online) XRD of imprinted (a) and non-imprinted (b) films.

Table II. Area ratio of O vacancy/M-O bond.

	Non-imprinted	Imprinted
In ₂ O ₃	0.8	<2.3
ITO via Sn(acac) ₂	1.2	≈1.5
ITO via SnCl ₂	1.3	≈1.3

vacancies. The values of O vacancy/M-O bond are shown in the top right-hand side of Fig. 11 are presented in Table II.

From Fig. 11, it is evident that for the imprinted In₂O₃ film, the peak area ratio O vacancy/M-O bond is as large as 2.3, while for the non-imprinted case it is 0.8. As oxygen vacancies are responsible for free carriers in In₂O₃,²⁷ the structure is deformed during imprinting, leading to more oxygen vacancies. A similar analysis was conducted in Refs. 31 and 32, where the former reported that, as the oxygen content increases, the carrier concentration decreases and the latter showed that as the oxygen content increases, the O vacancy/M-O bond ratio decreases. As explained above, the structure of ITO does not deform much during imprinting, so the O vacancy/M-O bond ratio is similar for imprinted and non-imprinted samples in the case of ITO. Hence, the carrier concentration remains almost the same for ITO films.

Finally, the crystalline properties were characterized by XRD. Figures 12(a) and 12(b) show the XRD results for the imprinted and non-imprinted In₂O₃ and ITO films, respectively, with almost no peaks observed for imprinted In₂O₃ and ITO films, suggesting the imprinted films are amorphous in nature. In contrast, (222) and (400) diffraction peaks were found for non-imprinted films, indicating that the imprinting process prevents the crystallization of In₂O₃, probably due to the large residual carbon content. This also corresponds to the experimental result that the mobility of imprinted film was smaller than that of non-imprinted films.

4. Conclusion

n-RP is a resist-free direct patterning technique to achieve patterns in metal-oxide precursor gels in the nanoscale range, allowing precise shape control. During n-RP, the precursor gel is deformed by the application of the appropriate imprinting temperature and pressure. The addition of Sn to In₂O₃ (i.e. ITO) degrades the n-RP properties because the $\tan \delta$ value of ITO is smaller than that of In₂O₃. Consequently, the electrical properties of imprinted ITO films are not altered as much as those of non-imprinted ITO films, but are greatly affected in the case of imprinted In₂O₃ compared with the non-imprinted In₂O₃ films. The Hall mobility of imprinted In₂O₃ decreases due to the trapped carbon, as confirmed by SIMS measurements which showed that even after annealing at 600 °C for 1 h, there was more carbon in the imprinted In₂O₃ than in non-imprinted In₂O₃. An increase in the carrier concentration in imprinted films is due to the increase in oxygen vacancies in In₂O₃ after imprinting, as confirmed by XPS studies.

Acknowledgments

The authors would like to thank Mr Akio Miyazato of the JAIST for the mass-spectroscopic measurements. The support of Professor Masayuki Yamaguchi of the School of Materials Science, JAIST for measuring the viscoelastic properties of the gel is also appreciated. The authors would also like to thank Assistant Professor Phan Tue for his continuous support. The authors are grateful for the financial support from the Nippon Sheet Glass Foundation for Materials Science and Engineering, and the Mitani Foundation for Research and Development.

- 1) M. Mashayekhi, A. Conde, T. N. Ng, P. Mei, E. Ramon, C. Martinez-Domingo, A. Alcalde, L. Teres, and J. C. Bordoll, *J. Disp. Technol.* **11**, 658 (2015).
- 2) G. D. Martin, S. D. Hoath, and I. M. Hutchings, *J. Phys. Conf. Ser.* **105**, 012001 (2008).
- 3) T. R. Hebner, C. C. Wu, D. Marcy, M. H. Lu, and J. C. Sturm, *Appl. Phys. Lett.* **72**, 519 (1998).
- 4) T. Kaneda, D. Hirose, T. Miyasako, P. T. Tue, Y. Murakami, S. Kohara, J. Li, T. Mitani, E. Tokumitsu, and T. Shimoda, *J. Mater. Chem. C* **2**, 40 (2014).
- 5) E. Sowade et al., *Sci. Rep.* **6**, 33490 (2016).
- 6) Y. Takeda, K. Hayasaka, R. Shiwa, K. Yokosawa, T. Shiba, M. Mamada, D. Kumaki, K. Fukuda, and S. Tokito, *Sci. Rep.* **6**, 25714 (2016).
- 7) J. Branson, J. Naber, and G. Edelen, *IEEE Trans. Educ.* **43**, 257 (2000).
- 8) S. Khan, L. Lorenzelli, and R. S. Dahiya, *IEEE Sens. J.* **15**, 3164 (2015).
- 9) J. Suikkola, T. Björninen, M. Mosallaei, T. Kankkunen, P. Iso-Ketola, L. Ukkonen, J. Vanhala, and M. Mäntysalo, *Sci. Rep.* **6**, 25784 (2016).
- 10) T. Arai, N. Sato, K. Yamaguchi, M. Kawasaki, M. Fujimori, T. Shiba, M. Ando, and K. Torii, *Japan. J. Appl. Phys.* **46**, 2700 (2007).
- 11) B. E. Park, H. Ishiwara, M. Okuyama, S. Sakai, and S. M. Yoon, *Ferroelectric-Gate Field Effect Transistor Memories* (Springer, Netherlands, 2016) 1st ed., p. 344.
- 12) K. Haga, Y. Kamiya, and E. Tokumitsu, *Japan. J. Appl. Phys.* **57**, 02CB14 (2018).
- 13) J. Huang, B. Yan, A. Faghihnejad, H. Xu, and H. Zeng, *Korea-Aust Rheol. J.* **26**, 3 (2014).
- 14) D. Hirose, H. Koyama, K. Fukada, Y. Murakami, K. Satou, S. Inoue, and T. Shimoda, *Phys. Status Solidi. A* **214**, 1600397 (2017).
- 15) P. T. Tue, K. Fukada, and T. Shimoda, *Appl. Phys. Lett.* **111**, 223504 (2017).
- 16) K. Nagahara, D. Hirose, J. Li, J. Mihara, and T. Shimoda, *Ceram. Int.* **42**, 7730 (2016).

- 17) H. Koyama, K. Fukada, Y. Murakami, P. T. Tue, S. Tanaka, S. Inoue, and T. Shimoda, *SID Int. Symp. Dig. Tec.* **45**, 979 (2014).
- 18) M. Terai, K. Fujita, and T. Tsutsui, *Japan. J. Appl. Phys.* **44**, 1059 (2005).
- 19) A. Ginsburg, M. Priel, H. N. Barad, D. A. Keller, E. Borvick, K. Rietwyk, A. Kama, S. Meir, A. Y. Anderson, and A. Zaban, *Sol. Energy Mater. Sol. Cells* **179**, 254 (2018).
- 20) D. J. Seo, J. P. Shim, S. B. Choi, T. H. Seo, E. K. Suh, and D. S. Lee, *Opt. Express* **20**, A991 (2012).
- 21) R. M. Pasquarelli, C. J. Curtis, A. Miedaner, M. F. A. van Hest, R. P. O. Hayre, and D. S. Ginley, *Inorg. Chem.* **49**, 5424 (2010).
- 22) M. Epifani, R. Diaz, J. Arbiol, P. Siciliano, and J. R. Morante, *Chem. Mater.* **28**, 840 (2006).
- 23) LibreTexts (2014), Infrared Spectroscopy Absorption Table [https://chem.libretexts.org/Reference/Reference_Tables/Spectroscopic_Parameters/Infrared_Spectroscopy_Absorption_Table].
- 24) M. Thirumoorthi and J. T. J. Prakash, *J. Asian Ceram. Soc.* **4**, 124 (2016).
- 25) M. Moradi-Haji Jafan, M.-R. Zamani-Meymian, R. Rahimi, and M. Rabbani, *J. Nanostruct. Chem.* **4**, 89 (2014).
- 26) A. M. Sayed and S. M. Yakout, *J. Res. Nanotechnol.* **2016**, 1 (2016).
- 27) A. Facchetti and T. J. Marks, *Transparent Electronics* (Wiley, Chichester, 2010) 1st ed., p. 8.
- 28) G. Frank, H. Kostlin, and A. Rabenau, *Phys. Status Solidi A* **52**, 231 (1979).
- 29) N. Nadaud, N. Lequeux, and M. Nanot, *J. Solid State Chem.* **135**, 140 (1998).
- 30) W. C. Chang, C. H. Kuo, C. C. Juan, P. J. Lee, Y. L. Chueh, and S. J. Lin, *Nanoscale Res. Lett.* **7**, 684 (2012).
- 31) S. M. Kim, H. W. Choi, K. H. Kim, S. J. Park, and H. H. Yoon, *J. Korean Phys. Soc.* **55**, 1996 (2009).
- 32) W. F. Wu and B. S. Chiou, *Semicond. Sci. Technol.* **11**, 196 (1999).

BRIEF NOTES

Effect of trichloroethylene enhancement on deposition rate of low-temperature silicon oxide films by silicone oil and ozone

To cite this article: Susumu Horita and Puneet Jain 2017 *Jpn. J. Appl. Phys.* **56** 088003

View the [article online](#) for updates and enhancements.

Related content

- [Low-Temperature Deposition of Silicon Oxide Film from the Reaction of Silicone Oil Vapor and Ozone Gas](#)
Susumu Horita, Koichi Toriyabe and Kensuke Nishioka
- [Spectroscopic studies on preparation of silicon oxide films by PECVD using organosilicon compounds](#)
Y Inoue and O Takai
- [Liquid-Phase Deposition of Silicon-Dioxide Films using Tetra-Ethyl Orthosilicate](#)
Koh-ichi Usami, Shin Hayashi, Yasutaka Uchida et al.

Recent citations

- [Highly effective removal of OH bonds in low-temperature silicon oxide films by annealing with ammonia gas at a low temperature of 175 °C](#)
Susumu Horita
- [Dependences of deposition rate and OH content on concentration of added trichloroethylene in low-temperature silicon oxide films deposited using silicone oil and ozone gas](#)
Susumu Horita and Puneet Jain



Effect of trichloroethylene enhancement on deposition rate of low-temperature silicon oxide films by silicone oil and ozone

Susumu Horita* and Puneet Jain

School of Materials Science, Japan Advanced Institute of Science and Technology, Nomi, Ishikawa 923-1292, Japan

*E-mail: horita@jaist.ac.jp

Received May 2, 2017; accepted May 16, 2017; published online July 3, 2017

A low-temperature silicon oxide film was deposited at 160 to 220 °C using an atmospheric pressure CVD system with silicone oil vapor and ozone gases. It was found that the deposition rate is markedly increased by adding trichloroethylene (TCE) vapor, which is generated by bubbling TCE solution with N₂ gas flow. The increase is more than 3 times that observed without TCE, and any contamination due to TCE is hardly observed in the deposited Si oxide films from Fourier transform infrared spectra. © 2017 The Japan Society of Applied Physics

The low-temperature deposition of silicon oxide films is desired for the fabrication of not only thin film transistors (TFTs) on non-heat-resistant substrates¹⁾ but also interlayer dielectrics (ILD) in size-minimizing integrated circuits to suppress the disconnection of the interconnect metal, the redistribution of the dopant, and defect generation in the fabricated underlayer.²⁾ For low-temperature deposition, plasma-enhanced chemical vapor deposition (PECVD) has been widely carried out as a practical method.^{1,3–6)} However, it requires an expensive system consisting of vacuum equipment and high power supply. Also, tetraethylorthosilicate [TEOS: Si(OC₂H₅)₄] vapor is commonly used as a deposition gas source.^{3–5)} On the other hand, previously, we reported on the deposition of low-temperature Si oxide films using silicone oil (SO) vapor as a deposition source and ozone O₃ gas at a temperature of 200 to 350 °C at atmospheric pressure without vacuum and pumping systems.^{7,8)} SO has advantages over TEOS; the price per unit volume of SO is lower than that of TEOS by about one order, and silicone is not only markedly thermally stable but also a safe material as opposed to TEOS, which is toxic especially to the human eye and throat.⁹⁾

A deposition mechanism for the silicon oxide film produced using SO and O₃ is described in our previous paper.⁸⁾ This mechanism is similar to that of the TEOS/O₃ system.^{10–13)} First, O₃ is decomposed thermally into O₂+O. Then, chemically very active O atoms react with the –CH₃ side groups of SO in the gas phase and intermediate products (precursors) are formed together with the by-products CO₂ and H₂O. –CH₃ side groups are substituted with hydroxyl –OH groups, and silanol bonds of Si–OH cover the sides of siloxane chains. The surface of a Si substrate or the deposited Si oxide film is terminated by –OH groups through exposure to O₃ gas and H₂O of a by-product. Finally, the –OH groups on the surface are eliminated by dehydration reaction with the –OH groups of the precursors, Si–OH (surface) + –OH (precursor) → Si–O–Si + H₂O. Then, a [–Si–O–Si–]_n network is constructed on the substrate and the deposition of Si oxide films continues.

However, the deposition rate of the Si oxide films using SO is very low at 3 nm/min,⁸⁾ which is not favorable for industrial application. To solve this problem or increase the deposition rate, we attempted to add a certain amount of trichloroethylene (C₂HCl₃: TCE) vapor together with SO and O₃ during deposition. It is well known that an acid catalyst is commonly used to enhance the dehydration reaction. For example, hydrochloric acid (HCl) is used for Fischer

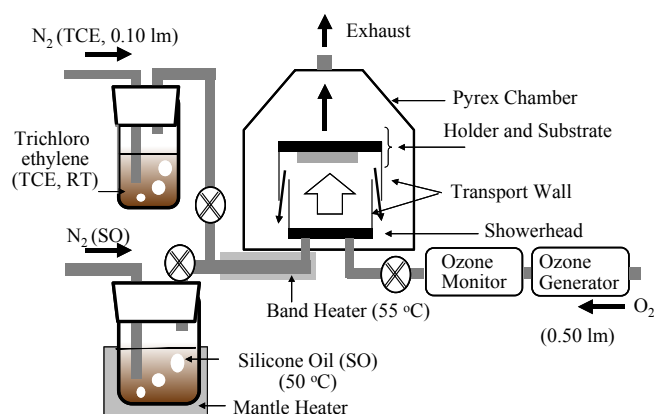


Fig. 1. (Color online) Schematic diagram of the APCVD system used in this study. The system consists of a vertical reactor, a substrate holder, a transport wall, a showerhead, and a reactant gas supply system. The N₂ gas flow rate is 0.25, 0.3, or 0.35 lm for SO and the substrate temperature ranges from 160 to 220 °C.

esterification reaction.¹⁴⁾ Since H and Cl dissolved from TCE owing to the chemically active O₃ might act as an acid, it is expected that the TCE vapor will enhance the dehydration reaction, markedly increasing the deposition rate.

In this paper, we report the results obtained by adding TCE vapor during the low-temperature deposition of Si oxide films, and show a marked improvement in deposition rate, which is about 3 times that observed without TCE.

Figure 1 shows a schematic diagram of the deposition system used in this study. The system has a vertical reactor of atmospheric-pressure (AP) CVD instead of the horizontal type used previously.⁸⁾ Using this system, film thickness uniformity was much improved, compared with that observed with the previous horizontal reactor. For example, the difference in thickness on a 4 inch Si wafer is about ±2% for an average Si oxide film thickness of 140 nm. However, the deposition rate is still lower than 5 nm/min at 200 °C as shown later. The substrate was held face down on a 100-mm-diameter stainless steel holder. As silicone oil, decamethylcyclotetrasiloxane (C₁₀H₂₀O₄Si₄) was used with a kinematic viscosity of 4.0 mm²/s. The vapor was generated by the N₂ gas bubbling of SO, which was heated using a mantle heater to a temperature of 50 °C. The gas flow rate of N₂ for SO vapor, N₂(SO), was 0.25 to 0.35 lm (liters per minute at 25 °C). We also added TCE vapor, which was generated by bubbling with N₂ gas with a flow rate of 0.10 lm at room temperature, and then introduced it into the chamber together with SO vapor.

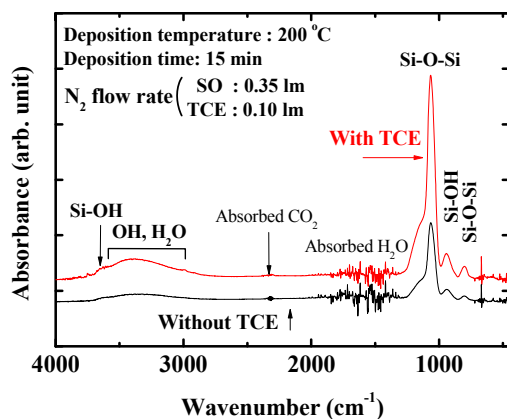


Fig. 2. (Color online) Typical FT-IR spectra of 70- and 196-nm-thick silicon oxide films deposited with and without TCE, respectively, for the deposition time of 15 min at the substrate temperature of 200 °C.

Both gases were flown through a 1/4-in.-diameter stainless steel tube heated using a band heater to about 55 °C to prevent the condensation of SO vapor. O₃ was generated using a silent electric discharge from 99.9995% O₂ gas with a flow rate of 0.50 l/min and the O₃ concentration was ~150 g/m³. The SO+TCE vapor and O₃+O₂ gases were introduced individually into the showerhead, where the two groups of gases were mixed. Then, they were directed towards the heated substrate along the stainless steel transport wall with a diameter of ~110 mm. The distance between the showerhead and the substrate was ~100 mm. The films were deposited for 5, 10, or 15 min at a substrate temperature of 160, 180, 200, or 220 °C. The entire outside of the reactor chamber was made of Pyrex glass.

Substrates were n-type (111) single crystals with a resistivity of 5–15 Ω cm. Before setting a substrate on a holder, it was chemically cleaned in hot acid solution and dipped in dilute HF solution to remove Si oxide. The thicknesses of the as-deposited films were measured by ellipsometry using a He–Ne laser beam with a wavelength of 632.8 nm. In the case of a film with a thickness of less than 25 nm, for simplicity, the refractive index was assumed to be 1.44. Although the refractive index of the silicon oxide film was not real, the error due to this was estimated to be roughly less than 3%, judging from the results obtained by a more accurate measurement method with spectroscopic ellipsometry. The molecular structures of the as-deposited films were analyzed from Fourier transform infrared spectroscopy (FT-IR) spectra with a resolution of 1 cm^{−1}.

Figure 2 shows the typical FT-IR spectra of 194- and 70-nm-thick silicon oxide films deposited at 200 °C with and without TCE, respectively, where the N₂ flow rate for SO is 0.35 l/min and the deposition time is 15 min. The spectral shape is similar to those obtained previously using the horizontal furnace.⁸⁾ The peaks at ~800 and 1070 cm^{−1} are identified as absorptions due to the bending (TO₂) and asymmetric stretching (TO₃) modes of the Si–O–Si bond, respectively. This indicates that the silicon oxide film is almost stoichiometric. However, peaks due to the Si–OH and H–OH bonds are observed at around 960 and 3650, and ~3300 cm^{−1}, respectively, indicating that the oxide films contain a relatively large amount of water. This observation of the OH bond is the same as that previously reported. It is considered

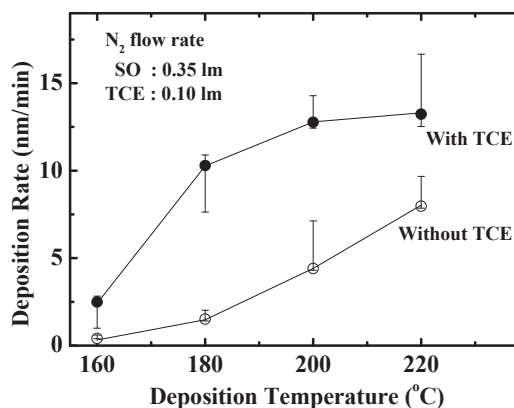


Fig. 3. Comparison of deposition temperature dependences of deposition rate obtained with and without TCE, where the temperature ranges from 160 to 220 °C and N₂ (SO) is 0.35 l/min. The plots and error bars indicate the averages and ranges of deposition rate, respectively, among the 3 deposition times of 5, 10, and 15 min.

that the OH bonds incorporated in the films are mainly from the silanol bonds of Si–OH of the precursors where the dehydration reaction does not occur during the deposition with some possibility in statistical thermodynamics. By comparing the two spectra, the peak intensity due to the Si–O–Si bond for TCE is observed to be markedly higher than that obtained without TCE. This indicates that adding TCE increases the deposition rate of Si oxide films as expected previously. Furthermore, a peak related to chlorine derived from TCE is hardly observed. This result indicates that TCE increases the Si oxide deposition rate, but negligibly affects the chemical composition of the films.

Figure 3 shows the comparison of the temperature dependences of deposition rate obtained with (closed circles) and without (open circles) TCE, where the temperature ranges from 160 to 220 °C and N₂ (SO) is 0.35 l/min. The data plots and error bars indicate the averages and ranges of deposition rate, respectively, among the three deposition times of 5, 10, and 15 min. It is seen clearly from Fig. 3 that, in the temperature range, the deposition rate is higher with TCE than without TCE, as shown in Fig. 2. It is also found that the deposition rate with TCE saturates at the higher deposition temperature, while that without TCE increases largely with the temperature in a nonlinear fashion. This will be discussed in detail later.

Figure 4 shows the dependence of deposition rate on deposition temperature for the N₂(SO) flow rates of 0.35 (circles), 0.30 (squares), and 0.25 (triangles) l/min with TCE, where the data for 0.35 l/min are the same as those in Fig. 3 and the error bars have the same meaning. It can be seen that, at any deposition temperature, decreasing the N₂(SO) flow rate leads to a reduction in deposition rate. This is because the feeding rate of SO vapor into the reaction chamber is proportional to the flow rate of N₂ required to bubble SO. Also, it is found that, as the deposition temperature increases above 200 °C, the deposition rate for any N₂ flow rate saturates as shown in Fig. 3 or tends to decrease with temperature. This can be explained on the basis of the gas phase and surface reactions. The gas phase reaction is a chemical reaction that occurs between gaseous reactants or SO + O₃ near the substrate surface but not on it. Thus, owing to this reaction, some

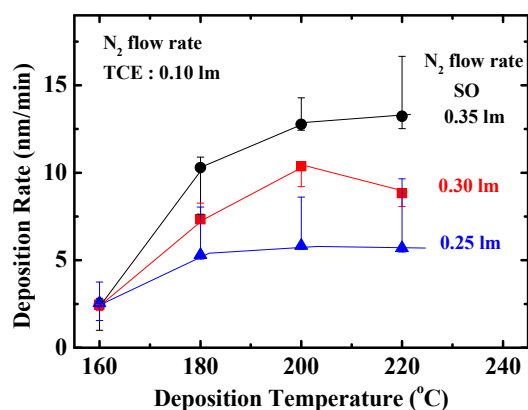


Fig. 4. (Color online) Dependence of deposition rate on the deposition temperature for the N_2 (SO) flow rates of 0.35 (circles), 0.30 (squares), and 0.25 (triangles) lm with TCE.

of the reactants are consumed before reaching the substrate. The surface reaction is a chemical reaction that occurs between the gaseous reactants on active sites of the substrate surface. As the temperature increases, the gas phase reaction becomes more pronounced as reported previously by other researchers.^{15–18} This is because, owing to the high-temperature radiation from the substrate holder, some reactant gases react near the substrate surface in the gas phase to produce intermediate species. In the case with TCE, since its vapor increases the deposition rate or enhances the chemical reaction, particularly the dehydration reaction, as shown in Figs. 2 and 3, the gas phase reaction must be promoted also, compared with that in the case without TCE. This is probably due to the fact that the promoted dehydration reaction occurs even at around 200 °C, at which it never occurs without TCE. Most of the SiO_2 particles formed in the gas phase through the promoted dehydration reaction probably do not contribute to deposition on the substrate. Thus, with an increase in deposition temperature, the actual deposition rate of Si oxide films on the substrate is reduced. As a result, the deposition rate saturates or slightly decreases with an increase in deposition temperature as shown in Figs. 3 and 4. In contrast, in the case without TCE, since the thermal energy from the heated substrate in this experiment is insufficient for chemical reaction among reactant gases, the deposition rate monotonically increases with the deposition temperature as shown in Fig. 3.

Although adding TCE during the deposition increases the deposition rate effectively as mentioned previously, its effect on the reduction in OH content seems to be smaller as shown in Fig. 2, which shows that the peaks due to the OH bond are much larger with TCE than without TCE. One of the reasons for this is the markedly larger thickness in the TCE case. Another reason might be that, as mentioned previously, since the residual OH bonds in a Si oxide film are mainly due to

the non-dehydration reaction between the silanols and OH bonds terminated at the substrate surface, a higher deposition rate could lead to a lower possibility in their dehydration reaction such that the number of unreacted OH bonds should become larger in the deposited film. However, at present, we hardly know not only the deposition rate dependence of the incorporation rate of OH bonds but also the effect of TCE on the reduction in incorporation rate in a deposited film. Thus, we will investigate them and report our results about this in the future.

In this study, we showed that adding TCE vapor markedly increases the deposition rate more than 3 times that observed without TCE for the low-temperature deposition of Si oxide films using silicone oil and ozone in an APCVD system, where the deposition temperature was around 200 °C. We found that TCE negligibly affects the chemical component of Si oxide or produces few amount of impurity in the films. Thus, we can conclude that adding TCE in the deposition gas source, e.g., organic silicon, is markedly effective in increasing the deposition rate of Si oxide films in a low deposition temperature range.

Acknowledgment This research is partially supported by JSPS KAKENHI Grant Number JP16K06257.

- 1) S. Higashi, D. Abe, S. Inoue, and T. Shimoda, *Jpn. J. Appl. Phys.* **40**, 4171 (2001).
- 2) M. M. Moslehi, R. A. Chapman, M. Wong, A. Paranjpe, H. N. Najm, J. Kuehne, R. L. Yeakley, and C. J. Davis, *IEEE Trans. Electron Devices* **39**, 4 (1992).
- 3) A. M. Mahajan, L. S. Patil, J. P. Bange, and D. K. Gautam, *Vacuum* **79**, 194 (2005).
- 4) Y. Nishi, T. Funai, H. Izawa, T. Fujimoto, H. Morimoto, and M. Ishii, *Jpn. J. Appl. Phys.* **31**, 4570 (1992).
- 5) N. Hirashita, S. Tokitoh, and H. Uchida, *Jpn. J. Appl. Phys.* **32**, 1787 (1993).
- 6) G. Mannino, R. Ruggeri, A. Alberti, V. Privitera, G. Fortunato, and L. Maiolo, *Appl. Phys. Express* **5**, 021103 (2012).
- 7) T. Toriyabe, K. Nishioka, and S. Horita, Proc. 13th Int. Display Workshops (IDW'06), 2006, p. 719.
- 8) S. Horita, K. Toriyabe, and K. Nishioka, *Jpn. J. Appl. Phys.* **48**, 035502 (2009).
- 9) H. Nakashima, K. Omac, T. Takebayashi, C. Ishizuka, and T. Uemura, *J. Occup. Health* **40**, 270 (1998).
- 10) T. Kawahara, A. Yuuki, and Y. Matsui, *Jpn. J. Appl. Phys.* **31**, 2925 (1992).
- 11) I. A. Shareef, G. W. Rubloff, M. Anderle, W. N. Gill, J. Cotte, and D. H. Kim, *J. Vac. Sci. Technol. B* **13**, 1888 (1995).
- 12) D. Cheng, K. Tsukamoto, H. Komiyama, Y. Nishimoto, N. Tokumasu, and K. Maeda, *J. Appl. Phys.* **85**, 7140 (1999).
- 13) S. Romet, M. F. Couturier, and T. K. Whidden, *J. Electrochem. Soc.* **148**, G82 (2001).
- 14) J. McMurry, *Fundamentals of Organic Chemistry* (Brooks/Cole, Belmont, CA, 2011) 7th ed., p. 339.
- 15) E. J. Kim and W. N. Will, *J. Cryst. Growth* **140**, 315 (1994).
- 16) K. Fujino, Y. Nishimoto, N. Tokumasu, and K. Maeda, *J. Electrochem. Soc.* **137**, 2883 (1990).
- 17) Y. Ikeda, Y. Numasawa, and M. Sakamoto, *J. Electron. Mater.* **19**, 45 (1990).
- 18) M. Ouyang, C. Yuan, R. J. Muisener, A. Boulares, and J. T. Koberstein, *Chem. Mater.* **12**, 1591 (2000).

REGULAR PAPERS

Dependences of deposition rate and OH content on concentration of added trichloroethylene in low-temperature silicon oxide films deposited using silicone oil and ozone gas

Recent citations

- [Highly effective removal of OH bonds in low-temperature silicon oxide films by annealing with ammonia gas at a low temperature of 175 °C](#)
Susumu Horita

To cite this article: Susumu Horita and Puneet Jain 2018 *Jpn. J. Appl. Phys.* **57** 03DA02

View the [article online](#) for updates and enhancements.



Dependences of deposition rate and OH content on concentration of added trichloroethylene in low-temperature silicon oxide films deposited using silicone oil and ozone gas

Susumu Horita* and Puneet Jain

School of Materials Science, Japan Advanced Institute of Science and Technology, Nomi, Ishikawa 923-1292, Japan

*E-mail: horita@jaist.ac.jp

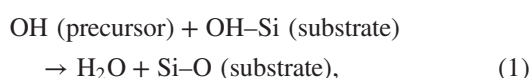
Received July 24, 2017; revised October 4, 2017; accepted October 12, 2017; published online January 23, 2018

We investigated the dependences of the deposition rate and residual OH content of SiO₂ films on the concentration of trichloroethylene (TCE), which was added during deposition at low temperatures of 160–260 °C with the reactant gases of silicone oil (SO) and O₃. The deposition rate depends on the TCE concentration and is minimum at a concentration of ~0.4 mol/m³ at 200 °C. The result can be explained by surface and gas-phase reactions. Experimentally, we also revealed that the thickness profile is strongly affected by gas-phase reaction, in which the TCE vapor was blown directly onto the substrate surface, where it mixed with SO and O₃. Furthermore, it was found that adding TCE vapor reduces residual OH content in the SiO₂ film deposited at 200 °C because TCE enhances the dehydration reaction. © 2018 The Japan Society of Applied Physics

1. Introduction

Low-temperature deposition of silicon oxide films is needed for the fabrication of not only thin-film transistors (TFTs) on non-heat-resistant substrates¹⁾ but also interlayer dielectrics (ILD) in size-minimizing integrated circuits to suppress the disconnection of the interconnect metal, the redistribution of the dopant, and defect generation in the fabricated under-layer.²⁾ For low-temperature deposition, plasma-enhanced chemical vapor deposition (PECVD) has been widely used in practice.^{1,3–6)} However, it requires an expensive system consisting of vacuum equipment and high power supply. Additionally, tetraethylorthosilicate [TEOS; Si(OC₂H₅)₄] vapor is commonly used as a deposition gas source.^{3–5)} However, we previously reported on the low-temperature deposition of Si oxide films using silicone oil (SO) vapor as a deposition source and ozone (O₃) gas at temperatures of 200–350 °C at atmospheric pressure without vacuum or pumping systems.^{7,8)} SO has advantages over TEOS; the price per unit volume of SO is lower than that of TEOS by about one order, and silicone is not only markedly thermally stable but also a safe material, whereas TEOS is toxic especially to the human eye and throat.⁹⁾

However, the rate of Si oxide film deposition using SO is very low at less than 5 nm/min,⁸⁾ which is not favorable for industrial application. To overcome this problem, we have reported recently that adding some amount of trichloroethylene (C₂HCl₃; TCE) vapor markedly increases the deposition rate to more than 3 times that without TCE during deposition in combination with SO and O₃ at deposition temperatures lower than 200 °C.¹⁰⁾ The increase in the deposition rate is caused by TCE-enhanced dehydration reaction between silanols of the precursors and OH bonds terminated at the surface of the substrate or deposited film, i.e.,



as determined on the basis of the previous reports on the deposition mechanism of the TEOS/O₃ system.^{11–14)} TCE may be decomposed into H and C among others because of the highly reactive O₃, and hydrochloric acid can be formed. Commonly, an acid is used as a catalyst to enhance the

dehydration reaction in an organic chemical solution, e.g., in the Fischer esterification reaction.¹⁵⁾

However, contrary to expectation, when the deposition temperature is increased to more than 200 °C, the deposition rate is suppressed or reduced despite the enhancement of the dehydration reaction.¹⁰⁾ This can be explained on the basis of the gas-phase and surface reactions.^{16–19)} The gas phase reaction is a chemical reaction that occurs between gaseous reactants or SO + O₃ near the substrate surface but not on it. Thus, owing to this reaction, some of the reactants are consumed without contributing to film deposition, which can reduce film deposition rate. The surface reaction is a chemical reaction that occurs between the gaseous reactants on active sites of the substrate surface, which contributes to film deposition.

On the other hand, it remains unclarified how the TCE concentration in reactant gas affects deposition rate. This investigation result will provide us with a method to increase the deposition rate further. Moreover, it is expected that the dehydration reaction enhancement due to TCE produces a low residual OH content in the deposited films. It has been reported that OH bond formation in low-temperature Si oxide films leads to the serious problems of high leakage current and low breakdown voltage.^{8,20–22)} Generally, low-temperature SiO₂ films prepared by CVD methods with organic silicon sources such as TEOS are more likely to contain a large amount of OH bonds when no special treatment is carried out, e.g., postdeposition annealing. Recently, we have reported some information on the TCE concentration dependence of deposition rate and the effect of TCE in reducing OH content in low-temperature SiO₂ films.²³⁾ However, the results and discussion are insufficient to further improve the deposition rate and reduce the residual OH content. Therefore, in this paper, with the addition of new data, the results are comprehensively reported and are discussed deeply from the viewpoints of the surface and gas-phase reactions of the reactants SO, O₃, and TCE. Furthermore, as a verification experiment for the gas-phase reaction, we blew TCE vapor on the substrate surface directly, where it mixed with the other reactant gases SO and O₃ flowing from elsewhere. Hereafter, this is referred to as “TCE direct flow”. Then, we measured film thickness and refractive index profiles at different distances from the outlet

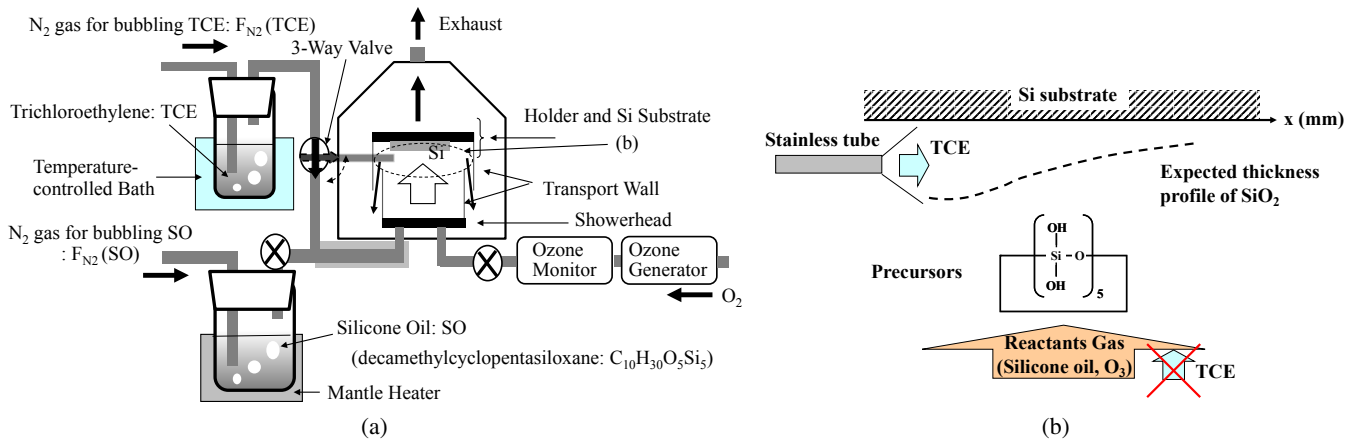


Fig. 1. (Color online) Schematic diagrams of the whole APCVD system (a) and the local line of the direct TCE flow (b) used in this research. In (a), the N_2 gas flow rate is 0.25 or 0.35 l/min for SO ($C_{10}H_{30}O_5Si_5$) and the substrate temperatures range from 160 to 260 °C. The TCE concentration is varied from ~ 0.10 to ~ 0.7 mol/m³ by controlling the TCE temperature from 5 to 32 °C and the N_2 gas flow rate, $F_{N_2}(TCE)$, from 0.03 to 0.1 l/min for TCE bubbling. The flow of the TCE vapor was divided into two lines with a three-way valve: directly to the substrate or to the chamber bottom.

of the TCE direct flow. The profiles clearly show a trace of the gas-phase reaction.

2. Experimental procedure

Figure 1(a) shows a schematic diagram of the deposition system used in this study. The system has a vertical reactor for atmospheric-pressure (AP) CVD. The details are mentioned in a previous paper.¹⁰⁾ The SO used was decamethylcyclopentasiloxane ($C_{10}H_{30}O_5Si_5$) heated to 50 °C using a mantle heater, and its vapor was generated by bubbling with N_2 gas. The flow rates of N_2 gas for the SO vapor, $F_{N_2}(SO)$, were 0.25 and 0.35 l/min (liters per minute at 25 °C). O_3 was generated using a silent electric discharge from 99.9995% O_2 gas at a flow rate of 0.50 l/min and the O_3 concentration was ~ 145 g/m³. The TCE vapor was generated by bubbling with N_2 gas, and it was then made to flow to one of the two lines, as shown in Fig. 1(a). One line led to the bottom of the chamber equipped with the SO vapor and $O_3 + O_2$ lines, and the other led to the substrate surface directly, i.e., TCE direct flow. In this case, the 1/4-in. diameter stainless tube was set ~ 5 mm above the substrate, as shown in Fig. 1(b). The gas flow direction to the chamber bottom or the substrate surface was controlled using the three-way valve shown in Fig. 1(a). The distance between the showerhead and the substrate was ~ 100 mm. The films were deposited for 10 min at substrate temperatures of 160–260 °C. The TCE concentration in the reactive chamber was varied from ~ 0.10 to ~ 0.7 mol/m³ by adjusting both the TCE solution temperature from 5 to 32 °C and the N_2 gas flow rate, $F_{N_2}(TCE)$, from 0.03 to 0.1 l/min for bubbling TCE. For TCE direct flow, the TCE flow rate was 0.0034 or 0.00065 l/min. The TCE concentration on the substrate surface is not uniform in this case because the TCE vapor immediately and randomly diffuses inside the reaction chamber after its release from the tube. Assuming that the TCE vapor is distributed uniformly in the reaction chamber, the concentrations at the TCE flow rates of 0.0034 and 0.00065 l/min are calculated to be 0.15 and 0.03 mol/m³, respectively. The detailed calculations of the TCE concentration and flow rate are described in Appendix.

Substrates were n-type (111) single crystals with resistivities of 5–15 Ω cm. Before setting a substrate on a holder, it was chemically cleaned in a hot acid solution and dipped in a

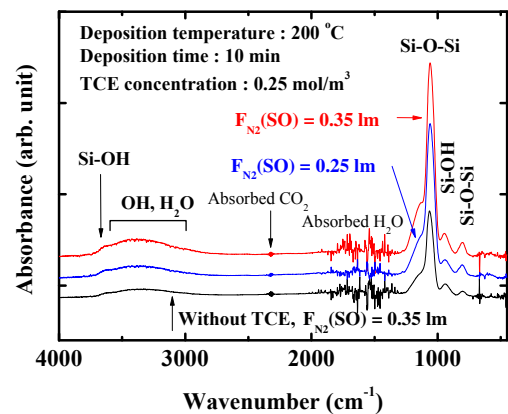


Fig. 2. (Color online) Typical FT-IR spectra of silicon oxide films deposited with and without TCE, where the TCE concentration is 0.25 mol/m³. The N_2 gas flow rates for bubbling SO, $F_{N_2}(SO)$, are 0.25 (with TCE) and 0.35 (with and without TCE) l/min.

dilute HF solution to remove Si oxide. The thicknesses and refractive indexes of the as-deposited films were measured by ellipsometry using a He–Ne laser beam with a wavelength of 632.8 nm. For the TCE bottom flow method, three points were measured on a 20×10 mm² substrate, which were near each edge and the center along the length of the substrate. For the TCE direct flow, points every 1.5–3.0 mm apart were measured on a $\sim 20 \times 60$ mm² substrate along the length. The molecular structures of the as-deposited films were analyzed from Fourier transform infrared spectroscopy (FT-IR) spectra with a resolution of 1 cm^{−1}.

3. Results

Figure 2 shows the typical FT-IR spectra of the silicon oxide films deposited at 200 °C with TCE (top and middle curves) and without TCE (bottom curve) as a reference. The $F_{N_2}(SO)$ values are 0.25 (middle curve) and 0.35 l/min (upper and bottom curves), and the TCE concentration is 0.25 mol/m³ for both $F_{N_2}(SO)$ values. The peaks at ~ 800 and 1070 cm^{−1} are identified as absorptions due to the bending (TO_2) and asymmetric stretching (TO_3) modes of the Si–O–Si bond, respectively.^{24–27)} This indicates that the silicon oxide films contain few hydrocarbon bonds from the deposition source of

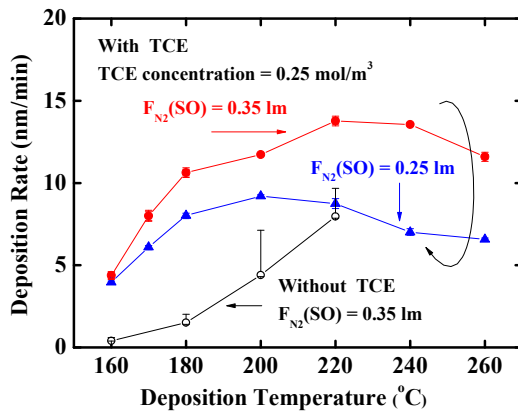


Fig. 3. (Color online) Deposition temperature dependences of deposition rate obtained with and without TCE, where the temperatures range from 160 to 260 °C, and TCE concentration is 0.25 mol/m³. $F_{N_2(SO)}$ with and without TCE are 0.25 and 0.35, and 0.35 lm, respectively. The plots and error bars indicate the averages and deposition rate ranges, respectively, among 6 measurement points for the two samples.

SO and that their chemical composition is almost the same as that of thermal oxide films. However, peaks due to the Si–OH bonds appear at around 960 and 3650, and those due to the H–OH bonds appear at $\sim 3300\text{ cm}^{-1}$, which are very often observed in films deposited by common low-temperature deposition methods using organic silicon deposition sources without any post-treatment.^{5,11,20,21,28,29} By comparing the spectra with and without TCE at $F_{N_2(SO)} = 0.35\text{ lm}$, it can be seen clearly that the peak intensities due to the Si–O–Si bond are markedly higher with TCE than without TCE. This is valid even for the lower $F_{N_2(SO)}$ of 0.25 lm, which supplies less Si source than $F_{N_2(SO)} = 0.35\text{ lm}$. This result suggests that adding TCE should increase the deposition rate of Si oxide films markedly.

Figure 3 shows the temperature dependences of deposition rates obtained with (closed circles and triangles) and without (open circles) TCE (as a reference), where the temperatures range from 160 to 260 °C and the TCE concentration is 0.25 mol/m³. The $F_{N_2(SO)}$ values with (closed circles and triangles) and without TCE (open circles) are 0.25 and 0.35, and 0.35 lm, respectively. The data plots and error bars indicate the averages and ranges of deposition rate, respectively, among all the measurement points. It can be seen from Fig. 3 that, at temperatures lower than 220 °C, the deposition rate is higher with TCE than without TCE. For the samples with TCE, the deposition rates at $F_{N_2(SO)} = 0.35\text{ lm}$ are always larger than those at $F_{N_2(SO)} = 0.25\text{ lm}$ at any deposition temperature because the Si source supply for the former is larger than that for the latter. Also, the deposition rates with TCE at both $F_{N_2(SO)}$ values saturate at higher deposition temperatures while that without TCE increases rapidly with temperature. These phenomena are almost the same as those observed in a previous study where TCE concentration was not controlled, which can be explained by surface and gas-phase reactions.¹⁰

Figure 4 shows the dependences of deposition rate on TCE concentration for the $N_2(SO)$ flow rates of 0.35 (circles) and 0.25 (triangles) lm,²³ where the data plot marks and error bars have the same meanings as those in Fig. 3. The deposition rate of $\sim 4.4\text{ nm/min}$ without TCE is shown as a broken solid line for reference. It is found from this result that

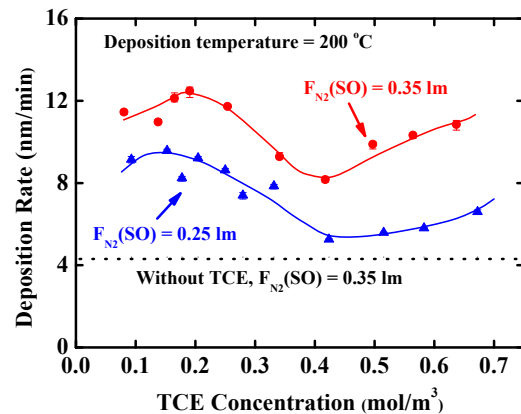


Fig. 4. (Color online) Dependence of deposition rate on TCE concentration for the $F_{N_2(SO)}$ of 0.35 (circles) and 0.25 (triangles) lm at the deposition temperature of 200 °C. The dotted line indicates the deposition rate without TCE as a reference.²³ The plots and error bars have the same meanings as those in Fig. 3.

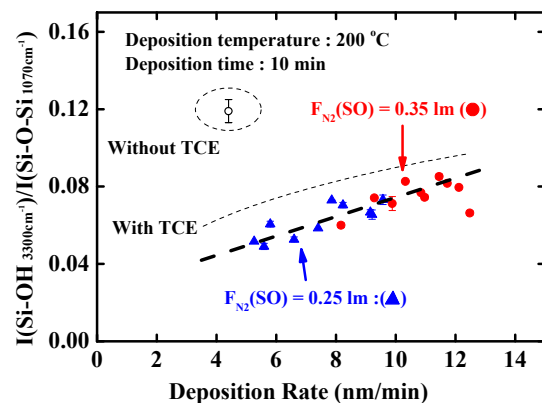


Fig. 5. (Color online) Dependence of deposition rate on relative OH content in the deposited films for $F_{N_2(SO)} = 0.25$ (closed triangles) and 0.35 (closed circles) lm with TCE. As a reference, the open circle indicates the data without TCE. The thick broken line is a guide for the eye. The plots and error bars indicate the averages and ranges of ratios, respectively, among two or more measurement samples.²³

the deposition rate with TCE at $F_{N_2(SO)} = 0.35\text{ lm}$ at any TCE concentration is more than twice that without TCE. Even at the smaller $F_{N_2(SO)} = 0.25\text{ lm}$, the deposition rates with TCE are higher than that without TCE. It can be seen, also, that the deposition rates depend on the TCE concentration, and the TCE concentration of the minimum deposition rate is approximately 0.4 mol/m³. This result indicates that the TCE concentration affects the chemical reaction between SO and O₃. This is discussed in more detail in Sect. 4.

To quantify OH content in the deposited SiO₂ films, we used peak intensity ratios at ~ 3400 and $\sim 1070\text{ cm}^{-1}$ in the FT-IR spectra, which are representative of the H–OH and Si–O–Si bond vibration modes, respectively. The intensity ratio gives us the relative number of OH bonds in deposited SiO₂ films. Figure 5 shows the deposition rate dependence of relative OH content in the deposited films.²³ The closed triangles and circles under the broken line show the data for $F_{N_2(SO)} = 0.25$ and 0.35 lm, respectively, with TCE, and the open circle enclosed with a broken circle shows the data for deposition without TCE. As can clearly be seen from Fig. 5,

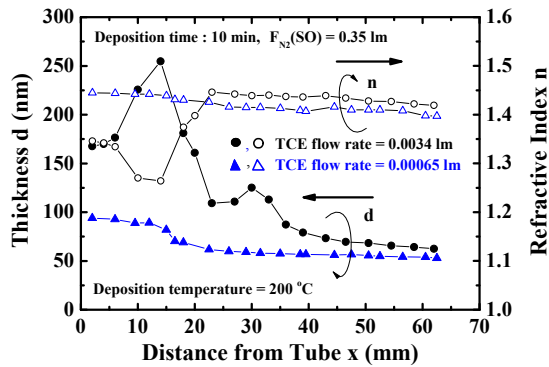


Fig. 6. (Color online) Film thickness d (closed) and refractive index n (open) profiles as functions of the distance x from the tube outlet for the TCE flow rates of 0.0034 (circles) and 0.00065 (triangles) lm. The deposition time is 10 min, the deposition temperature is 200 °C, and the N_2 gas flow rate for bubbling SO, $F_{N_2(SO)}$, is 0.35 lm.

the OH contents with TCE are much smaller than that without TCE. This means that the addition of TCE to the gas source is very effective in reducing OH content in the deposited SiO_2 films because of TCE-enhanced dehydration reaction. Furthermore, it can notice that the OH content in the SiO_2 films deposited with TCE is roughly proportional to the deposition rate although the data are somewhat scattered. Also, the data for deposition with TCE can be divided roughly into two groups in terms of the source gas flow rate, i.e., $F_{N_2(SO)} = 0.25$ and 0.35 lm. Generally, the OH content for the $F_{N_2(SO)} = 0.35$ lm group is larger than that for the 0.25 lm group since the deposition rate for $F_{N_2(SO)} = 0.35$ lm is on average about 1.5 times higher than that for $F_{N_2(SO)} = 0.25$ lm. The residual OH bonds in a Si oxide film are mainly due to the nondehydration reaction between silanols of the precursors and OH bonds terminated at the substrate surface, which has a statistical thermodynamic possibility of occurring. The probability of the dehydration reaction may be reduced if the deposition rate increases because of a shorter reaction time. Therefore, the number of unreacted OH bonds or the residual OH content in the deposited film is approximately proportional to the deposition rate as shown in Fig. 5. Furthermore, no TCE concentration dependence of residual OH content was observed clearly, and the data are not shown here. This is probably because OH content is governed mainly by deposition rate as shown in Fig. 5.

4. Discussion

As mentioned above, TCE enhances the dehydration reaction so that Si oxide formation is promoted on the substrate surface even at temperatures lower than 200 °C. This effect may promote the dehydration reaction in the gas phase during the transport of reactant gases and precursors toward the substrate. In order to confirm whether the gas-phase reaction really does occur in our experiment or not, we performed the experiment shown in Fig. 1(b). As expected, film thickness decreases with the distance x from the outlet of the tube exponentially because of gas diffusion. Figure 6 shows the film thickness (left) and refractive index (right) profiles as functions of the distance x from the tube outlet for 10 min deposition at 200 °C, where $F_{N_2(SO)} = 0.35$ lm, and the TCE flow rates, F_{TCE} , are 0.0034 (circles) and 0.00065 (triangles) lm. It can be seen that, under both conditions, the film

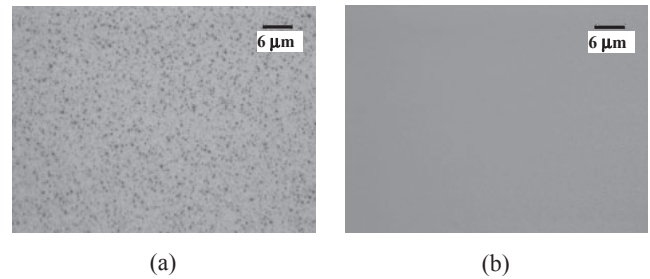


Fig. 7. Nomarski optical micrographs of the surface regions at $x \approx 10$ (a) and ~ 40 mm (b) of the sample with the TCE flow rate = 0.0034 lm in Fig. 6.

thicknesses generally decreases with distance as predicted. The thickness for $F_{TCE} = 0.0034$ lm is larger than that for $F_{TCE} = 0.00065$ lm in spite of the same supply rate of the SO deposition source, $F_{N_2(SO)} = 0.35$ lm, because the supply of TCE is much larger. In both cases, the asymptotic values at large distances (x) appear to approach about 50 nm, which is close to the value obtained without TCE, as shown in Figs. 3 and 4. This is probably because, at large distances, the TCE concentration is much reduced because of the random and fast diffusion of TCE in the chamber. However, the thickness profile with the higher TCE flow rate has two peaks at $x \approx 15$ and 30 mm while that with the lower TCE flow rate shows a curve that smoothly declines with x . On the other hand, the distance dependence of the refractive index appears similar to that of film thickness with the exception that the refractive index is much lower around the first peak position of the film thickness for $F_{TCE} = 0.0034$ lm. According to the Lorentz–Lorenz model,^{30,31)} the refractive index is directly proportional to the density of the film. Since the refractive indexes shown in Fig. 6 are lower than 1.46 of thermal SiO_2 , it is considered that the film densities are also lower. In particular, the refractive indexes in the region of the thicker film, i.e., $x = 10$ –20 mm, are less than 1.3, which means that the film density is considerably lower in this region than in the other regions. This is experimentally supported by Figs. 7(a) and 7(b), which show Nomarski optical micrographs of the surface regions at $x \approx 10$ and 40 mm, respectively, in the sample with the TCE flow rate of 0.0034 lm in Fig. 6. From Fig. 7, it can be seen clearly that the surface at $x \approx 10$ mm is much rougher than that at $x \approx 40$ mm. This result seems to correspond well to the refractive index behavior shown in Fig. 6. Formation of surface roughness at $x \approx 10$ mm is further discussed later.

Now, we focus our discussion on the two peaks in deposition rate for $F_{TCE} = 0.0034$ lm. O_3 is decomposed thermally into $O_2 + O$ at temperatures of more than 150 °C,⁸⁾ which is highly possible near the substrate owing to heat irradiation from the holder, which is heated at 200 °C. Thus chemically, very active O atoms react with the $-CH_3$ side groups of SO in the gas phase during the transport from the chamber bottom, and the $-CH_3$ side groups are substituted with hydroxyl $-OH$ groups, and the silanol bonds of Si–OH cover the sides of siloxane chains. Then, precursors are formed. Furthermore, owing to the effect of TCE, it is possible that the dehydration reaction of OH between some precursors occurs in the gas phase, and SiO_2 particles are formed during the transport of the reactant gases before reaching the substrate. Increasing TCE concentration must

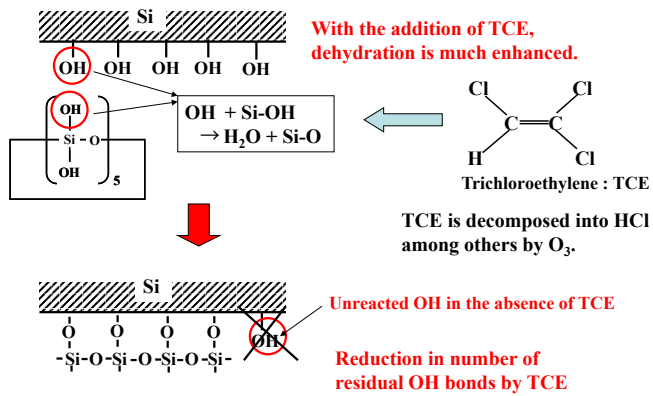
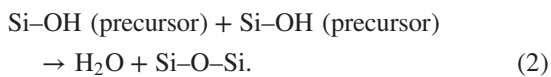


Fig. 8. (Color online) Deposition model of SiO_2 film, focusing on the TCE-enhanced dehydration reaction at the substrate surface. Enhanced dehydration reactions may reduce the number of unreacted OH bonds in deposited SiO_2 films.

promote the formation of SiO_2 particles in the gas phase. This gas-phase reaction is expressed by



Near the outlet tube, i.e., $x = 0$ to 15 mm, the TCE concentration is so high that heavy condensation or contraction of the precursors due to dehydration reactions between them occurs not only on the substrate surface but also in the gas phase as mentioned above. Therefore, SiO_2 particles are deposited loosely on the substrate, and then the film thickness becomes much larger as shown in Fig. 6. Also, the surface becomes too rough as shown in Fig. 7(a), so that the density of the deposited Si oxide film is much lower than that of thermal silicon oxide as well as the refractive index. Accompanying this complex dehydration reaction, the density of the precursor in the gas phase is much reduced, which induces fast diffusion flow of the precursor from the region at $x \approx 25$ mm toward the tube outlet. As a result, the precursor density at $x \approx 25$ mm is also much reduced, and the film thickness profile has a minimum and a second peak at $x = 25$ and 30 mm, respectively, as shown in Fig. 6. This phenomenon might be hardly explained by the surface reaction without the involvement of the gas-phase reaction because high condensation and diffusion speeds of the precursor are needed for the formation of the two peaks in the thickness profile. Therefore, we can say that the gas-phase reaction is highly involved in the deposition mechanism when TCE is used.

Next, we discuss the TCE concentration dependence of deposition rate, as shown in Fig. 4, in particular, the minimum value and the fluctuation in deposition rate behaviors in the TCE concentration range from 0.2 to 0.5 mol/m³. Figure 8 shows a schematic model of SiO_2 film deposition with emphasis on the TCE-enhanced dehydration reaction at the substrate surface. The $-OH$ groups on the surface are eliminated by the dehydration reaction with the $-OH$ groups of the precursors, and then a $[-Si-O-Si-]_n$ network is constructed on the substrate and the deposition of Si oxide films continues. The elimination of OH groups is markedly promoted by adding TCE vapor, which leads to an increase in deposition rate, as shown above. However, if TCE concentration increases, e.g., to more than 0.2 mol/m³, the

gas-phase reaction may occur at non-negligible levels from the viewpoint of film deposition on the substrate. When the amount of SiO_2 formation due to the gas-phase reaction is much smaller than the amount needed for deposition thickness, we do not need to take the gas-phase reaction into account for the deposition model, and vice versa. Also, since the TCE gas flows from the chamber bottom, most SiO_2 particles formed in the gas phase probably do not contribute to film deposition on the substrate because of random scattering caused by the N_2 carrier gas and unreacted O_2 gas, with which the reaction chamber is almost filled. Furthermore, the SiO_2 particles have few OH bonds that act as a binding agents on the substrate surface through the dehydration reaction. This situation is different from the direct TCE flow shown in Figs. 1(b) and 6 because the distance from the SiO_2 formation location to the substrate in Figs. 1(a) and 4 is much larger than that in the direct TCE flow, which is less than 5 mm in Fig. 6. Therefore, the non-negligible amount of SiO_2 produced by the gas-phase reaction increases with the TCE concentration from 0.2 mol/m³, which causes a decrease in deposition rate, as shown in Fig. 4. However, when the TCE concentration becomes greater than about 0.4 mol/m³, the reversal reaction of Eq. (2) (or $Si-OH + Si-OH \leftarrow H_2O + Si-O-Si$) would occur more frequently according to the chemical equilibrium formula

$$\frac{[H_2O][Si-O-Si]}{[Si-OH]^2} = K, \quad (3)$$

where K is constant. Thus, since the dehydration reaction and consumption of precursors are suppressed to some level, even after increasing the TCE concentration further, precursors that are not reacted before arriving at the substrate can contribute to the surface reaction. As a result, the deposition rate increases gradually with TCE concentration, as shown in Fig. 4.

The above discussion on Fig. 4 is examined quantitatively. When the TCE concentration was 0.2 mol/m³, the concentrations of SO and O_3 used in the reaction chamber are calculated to be about 0.025 and 1.7 mol/m³, respectively. The calculation details are provided in Appendix. According to the chemical reaction between SO and O_3 given in Appendix [Eq. (A-5)], the O_3 concentration (C_{O_3}) of 1.7 mol/m³ is sufficient for reaction with SO at the concentration (C_{SO}) of 0.025 mol/m³ because the minimum required C_{O_3} is estimated as $0.025 \times 40 = 1.0$ mol/m³. Next, the necessary TCE concentration for the dehydration reaction is estimated roughly for $C_{SO} = 0.025$ mol/m³. Here, we assume that all 10 OH bonds of one precursor molecule shown in Fig. 8 undergo dehydration reactions and that the reaction per one OH bond is assisted by one HCl molecule produced from one TCE molecule. The estimated value is 0.25 mol/cm³ and roughly near the TCE concentration of 0.2 mol/m³ at which the deposition rate starts decreasing, as shown in Fig. 4. Therefore, it can be said that the above discussion on Fig. 4 is reasonable qualitatively.

Figure 6 shows that, with a deposition time of 10 min, the refractive index slightly decreases with decreasing film thickness or deposition rate except for the region of rates higher than ~ 15 nm/min. Also, it is found actually that, in the samples shown in Fig. 4, the refractive index decreases with

decreasing deposition rate, which is not shown here but is almost similar to the behavior shown in Fig. 6. Here, we will briefly discuss two possible mechanisms for this as follows: In addition to the gas-phase reaction, we can consider the possibility that a –OH-terminated Si on the film is released or desorbed from the surface by thermal energy, and this probability would increase with time assuming no overlayer deposition. Since a surface site without a –OH bond has a dangling bond, it may become a defective hole or void after successive deposition of an overlayer. That is, the –OH bonds are removed by not only dehydration reactions but also thermal desorption with a specific time constant. Therefore, the lower deposition rate induces a larger volume of voids or lower density of the deposited film so that the refractive index is reduced. The other possible mechanism involves surface roughness. The surface of the deposited Si oxide film is not perfectly smooth, and it might have a roughness of less than 10 nm despite presenting a macroscopically mirrorlike surface. The average refractive index may be affected or reduced somewhat by the volume ratio of the surface roughness to film bulk.³²⁾ This may occur, as shown in Fig. 6, if the volume ratio of roughness increases non-negligibly with decreasing film thickness. However, these mechanisms are speculative without clear theoretical or experimental evidence. In the future, we will investigate and discuss these mechanisms further.

5. Conclusions

In this study, we investigated the dependences of the deposition rate of SiO₂ films and residual OH content in the deposited films on the concentration of TCE, which was added during the deposition, mainly at temperatures below 200 °C, with the reactant gases SO and O₃. At the constant TCE concentration of 0.25 mol/m³, the deposition rate increases with deposition temperature up to 200 or 220 °C, but above that temperature, the deposition rate becomes saturated or decreases. Additionally, the deposition rate depends on the TCE concentration and is minimum at a concentration of ~0.4 mol/m³. The results of the deposition temperature and TCE concentration dependences can be explained by the concepts of surface and gas-phase reactions. Experimentally, we also revealed that the thickness profile is strongly affected by the gas-phase reaction, in which the TCE vapor was blown directly onto the substrate surface, where it mixed with SO and O₃. Furthermore, it was found that adding TCE vapor reduces residual OH content in the low-temperature deposition SiO₂ film because the TCE enhances the dehydration reaction. It is expected from these results that this TCE effect could be used for other deposition methods using organic deposition sources.

Acknowledgment

This research is partially supported by JSPS KAKENHI Grant Number JP16K06257.

Appendix

The saturated vapor pressure P_{SO} (Pa) of C₁₀H₃₀O₅Si₅ is given by the equation

$$\ln P_{SO} = A + \frac{B}{T} + C \cdot \ln T + D \cdot T^E, \quad (\text{A} \cdot 1)$$

where T is SO temperature (K), $A = 94.421$, $B = -10153$, $C = -10.031$, $D = 7.47649 \times 10^{-18}$, and $E = 6$.³³⁾ The saturated vapor pressure P_{TCE} (Pa) of TCE is given by the equation

$$\ln P_{TCE} = 5 \cdot \ln 10 \times \left(\frac{A - B}{T + C} \right), \quad (\text{A} \cdot 2)$$

where T is TCE temperature (K), $A = 3.55346$, $B = 974.538$, and $C = -85.811$.³⁴⁾ This is the Antoine equation with coefficients calculated from McDonald's data.³⁵⁾

The flow rates of SO (F_{SO}) and TCE (F_{TCE}) in the tube and before entering the reaction chamber are calculated using the equations

$$F_{SO} = \frac{P_{SO} \cdot F_{N_2}(\text{SO})}{P_0 - P_{SO}}, \quad (\text{A} \cdot 3)$$

$$F_{TCE} = \frac{P_{TCE} \cdot F_{N_2}(\text{TCE})}{P_0 - P_{TCE}}, \quad (\text{A} \cdot 4)$$

respectively. In this calculation, we assumed that the bubbling chambers of SO and TCE are in atmospheric pressure P_0 of 1 atm = 1.01×10^5 Pa, and that each flow rate is proportional to the saturation pressure of SO or TCE.

Using the same assumption for the reaction chamber, the SO (C_{SO}) and TCE (C_{TCE}) concentrations in the reaction chamber are calculated using the equations

$$C_{SO} = \frac{P'_{SO}}{RT_c} = \frac{P_0 \cdot F_{SO}}{RT_c \sum F}, \quad (\text{A} \cdot 5)$$

$$C_{TCE} = \frac{P'_{TCE}}{RT_c} = \frac{P_0 \cdot F_{TCE}}{RT_c \sum F}, \quad (\text{A} \cdot 6)$$

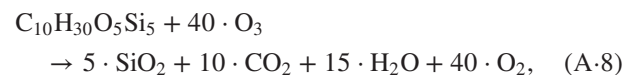
respectively, where $P'_{SO} = P_0 \cdot F_{SO} / \sum F$ and $P'_{TCE} = P_0 \cdot F_{TCE} / \sum F$ are the partial pressures of SO and TCE, respectively, T_c is temperature, $\sum F$ is the sum of the flow rates of N₂, O₂, O₃, SO, and TCE in the reaction chamber, and R is the gas constant. Also, in this calculation, the ideal gas equation $PV = nRT$ is used, where P is pressure, V is volume, and n is the number of moles.

Using the O₃ concentration C'_{O_3} before entering the reaction chamber, the O₃ concentration C_{O_3} in the reaction chamber is calculated using the equation

$$C_{O_3} = \frac{P_0 \cdot F_{O_3}}{RT_c \sum F} = \frac{C'_{O_2} \cdot F_{O_3}}{\sum F} = \frac{C'_{O_3} \cdot F_{O_2}}{\sum F}, \quad (\text{A} \cdot 7)$$

where F_{O_2} and F_{O_3} are the flow rates of O₂ and O₃, respectively, and C'_{O_2} is the O₂ concentration at P_0 before flowing into the ozone generator. In this calculation, the relations $C'_{O_2} = P_0 / (RT_c)$ and $C'_{O_2} : C'_{O_3} = F_{O_2} : F_{O_3}$ are used.

The chemical reaction between silicone oil (C₁₀H₃₀O₅Si₅) and O₃ can be expressed by



assuming that the final products are stable molecules of SiO₂, H₂O, CO₂, and O₂ from O₃.

- 1) S. Higashi, D. Abe, S. Inoue, and T. Shimoda, *Jpn. J. Appl. Phys.* **40**, 4171 (2001).
- 2) M. M. Moslehi, R. A. Chapman, M. Wong, A. Paranjpe, H. N. Najm, J. Kuehne, R. L. Yeakley, and C. J. Davis, *IEEE Trans. Electron Devices* **39**, 4 (1992).
- 3) A. M. Mahajan, L. S. Patil, J. P. Bange, and D. K. Gautam, *Vacuum* **79**, 194

- (2005).
- 4) Y. Nishi, T. Funai, H. Izawa, T. Fujimoto, H. Morimoto, and M. Ishii, *Jpn. J. Appl. Phys.* **31**, 4570 (1992).
- 5) N. Hirashita, S. Tokitoh, and H. Uchida, *Jpn. J. Appl. Phys.* **32**, 1787 (1993).
- 6) G. Mannino, R. Ruggeri, A. Alberti, V. Privitera, G. Fortunato, and L. Maiolo, *Appl. Phys. Express* **5**, 021103 (2012).
- 7) T. Toriyabe, K. Nishioka, and S. Horita, Proc. 13th Int. Display Workshops (IDW'06), 2006, p. 719.
- 8) S. Horita, K. Toriyabe, and K. Nishioka, *Jpn. J. Appl. Phys.* **48**, 035502 (2009).
- 9) H. Nakashima, K. Omae, T. Takebayashi, C. Ishizuka, and T. Uemura, *J. Occup. Health* **40**, 270 (1998).
- 10) S. Horita and P. Jain, *Jpn. J. Appl. Phys.* **56**, 088003 (2017).
- 11) T. Kawahara, A. Yuuki, and Y. Matsui, *Jpn. J. Appl. Phys.* **31**, 2925 (1992).
- 12) I. A. Shareef, G. W. Rubloff, M. Anderle, W. N. Gill, J. Cotte, and D. H. Kim, *J. Vac. Sci. Technol. B* **13**, 1888 (1995).
- 13) D. Cheng, K. Tsukamoto, H. Komiyama, Y. Nishimoto, N. Tokumasu, and K. Maeda, *J. Appl. Phys.* **85**, 7140 (1999).
- 14) S. Romet, M. F. Couturier, and T. K. Whidden, *J. Electrochem. Soc.* **148**, G82 (2001).
- 15) J. McMurry, *Fundamentals of Organic Chemistry* (Brooks/Cole, Belmont, CA, 2011) 7th ed., p. 339.
- 16) E. J. Kim and W. N. Will, *J. Cryst. Growth* **140**, 315 (1994).
- 17) K. Fujino, Y. Nishimoto, N. Tokumasu, and K. Maeda, *J. Electrochem. Soc.* **137**, 2883 (1990).
- 18) Y. Ikeda, Y. Numasawa, and M. Sakamoto, *J. Electron. Mater.* **19**, 45 (1990).
- 19) M. Ouyang, C. Yuan, R. J. Muisener, A. Boulares, and J. T. Koberstein, *Chem. Mater.* **12**, 1591 (2000).
- 20) Y. Nishi, T. Funai, H. Izawa, T. Fujimoto, H. Morimoto, and M. Ishii, *Jpn. J. Appl. Phys.* **31**, 4570 (1992).
- 21) M. Matsuura, Y. Hayashide, H. Kotani, and H. Abe, *Jpn. J. Appl. Phys.* **30**, 1530 (1991).
- 22) T. Ito, T. Matumoto, and K. Nishioka, *Surf. Coatings Technol.* **215**, 447 (2013).
- 23) P. Jain and S. Horita, Proc. 24th Int. Workshop Active-Matrix Flatpanel Displays and Devices (AM-FPD), 2017, p. 285.
- 24) F. L. Galeener, *Phys. Rev. B* **19**, 4292 (1979).
- 25) P. G. Pai, S. S. Chao, Y. Takagi, and G. Lucovsky, *J. Vac. Sci. Technol. A* **4**, 689 (1986).
- 26) G. Lucovsky, M. J. Manitini, J. K. Srivastava, and E. A. Irene, *J. Vac. Sci. Technol. B* **5**, 530 (1987).
- 27) J. T. Fitch, G. Lucovsky, E. Kobeda, and E. A. Irene, *J. Vac. Sci. Technol. B* **7**, 153 (1989).
- 28) M. Yoshimaru and T. Yoshie, *J. Electrochem. Soc.* **145**, 2847 (1998).
- 29) K. Murase, N. Yabumoto, and Y. Komine, *J. Electrochem. Soc.* **140**, 1722 (1993).
- 30) K. E. Oughstun and N. A. Cartwright, *Opt. Express* **11**, 1541 (2003).
- 31) L. Bányai and P. Gartner, *Phys. Rev. B* **29**, 728 (1984).
- 32) K. Imamura, D. Irishika, and H. Kobayashi, *J. Appl. Phys.* **121**, 013107 (2017).
- 33) D. N. Brooke, M. J. Crookes, D. Gray, and S. Robertson, *Environmental Risk Assessment Report: Decamethylcyclopentasiloxane* (Environment Agency, Bristol, U.K., 2009) p. 17.
- 34) NIST Chemistry WebBook, SRD 69 (National Institute of Standards and Technology, Gaithersburg, MD, 2016) [<http://webbook.nist.gov/cgi/cbook.cgi?ID=C79016&Mask=4&Type=ANTOINE&Plot=on>].
- 35) H. J. McDonald, *J. Phys. Chem.* **48**, 47 (1944).